Histone deacetylation and cytosine methylation compartmentalize heterochromatic regions in the genome organization of *Neurospora crassa*

Ashley W. Scadden[1], Alayne S. Graybill[1], Clayton Hull-Crew[1], Tiffany J. Lundberg[1], Nickolas M. Lande[1], and Andrew D. Klocko[1]*

[1]University of Colorado Colorado Springs, Department of Chemistry & Biochemistry, Colorado Springs, CO 80918, USA

***Corresponding Author:** Andrew D. Klocko, email: aklocko@uccs.edu

Author Contributions: A.W.S and A.D.K. designed research; A.W.S., A.S.G., C.H-C., T.J.L., N.M.L., and A.D.K. performed research; A.W.S., A.S.G., C.H-C., T.J.L., N.M.L., and A.D.K. analyzed data; and A.W.S., A.S.G., C.H-C., T.J.L., N.M.L., and A.D.K. wrote the paper.

Competing Interest Statement: The authors declare no conflict of interest.

Classification: Biological Sciences, Genetics

Keywords: histone deacetylation, HDAC, heterochromatin, Hi-C, cytosine methylation

Abstract

Chromosomes must correctly fold in eukaryotic nuclei for proper genome function. Eukaryotic organisms hierarchically organize their genomes: in the fungus *Neurospora crassa*, chromatin fiber loops compact into Topologically Associated Domain (TAD)-like structures that are anchored by the aggregation of silent heterochromatic regions. However, insufficient information exists on how histone post-translational modifications, including acetylation, impact genome organization. In Neurospora, the HCHC complex (comprised of the proteins HDA-1, CDP-2, HP1, CHAP) deacetylates heterochromatic regions, including centromeres: loss of individual HCHC members increases centromeric acetylation and cytosine methylation. Here, we evaluate the role of the HCHC complex on genome organization using chromosome conformation capture with high-throughput sequencing (Hi-C) in strains deleted of the *cdp-2* or *chap* genes. CDP-2 loss increases interactions between intra- and inter-chromosomal heterochromatic regions, while CHAP deletion decreases heterochromatic region compaction. Individual HCHC mutants exhibit different histone PTM patterns genome-wide: without CDP-2, heterochromatic H4K16 acetylation is increased, yet some heterochromatic regions lose H3K9 trimethylation, which increases interactions between heterochromatic regions; CHAP loss produces minimal acetylation changes but increases H3K9me3 enrichment in heterochromatin. Interestingly, deletion of the gene encoding the DIM-2 DNA methyltransferase in a *cdp-2* deletion background causes extensive genome disorder, as heterochromatic-euchromatic contacts increase despite additional H3K9me3 enrichment. Our results highlight how the increased cytosine methylation in HCHC mutants ensures heterochromatic compartmentalization when silenced regions are hyperacetylated.

Significance Statement

The mechanisms driving chromosome organization in eukaryotic nuclei, including in the filamentous fungus *Neurospora crassa*, are currently unknown, but histone post-translational modifications may be involved. Histone proteins can be acetylated to form active euchromatin while histone deacetylases (HDACs) remove acetyl marks to form silent heterochromatin; heterochromatic regions cluster and strongly interact in Neurospora genome organization. Here, we show that mutants lacking components of a heterochromatin-specific HDAC (HCHC) causes histone acetylation gains in heterochromatin genome-wide and increases contacts between distant heterochromatic loci. HCHC loss also impacts cytosine methylation, and in strains lacking both the HCHC and cytosine methylation, heterochromatic regions interact more with euchromatin. Our results suggest cytosine methylation normally functions to segregate silent and active loci when heterochromatic acetylation increases.

Main Text

Introduction

Chromosomal DNA must be correctly folded in a eukaryotic nucleus to ensure the proper genome function (1–3). Numerous DNA-templated processes, including transcription, mitosis/meiosis, and DNA repair, require precise compaction and organization of genomic DNA (1–6). Arguably, genome organization impacts gene expression the most, given the subnuclear compartmentalization of chromatin - the aggregate of proteins and DNA necessary for genome organization and function (1, 4, 7, 8). Here, in interphase cells, the more open, gene-rich, and transcriptionally active euchromatin is more centrally localized in the nucleus, while the densely compacted, transcriptionally silent heterochromatin associates at the nuclear periphery (9–12). This organization facilitates transcription regulation: the condensed heterochromatin at the nuclear periphery would be refractory to RNA polymerases, while the transcriptional machinery would presumably have greater access to the more open euchromatin (9, 13). In addition, long-range loops between promoters and distant regulatory sequences, including enhancers or silencers, are more apt to form with more open euchromatin (4, 8, 14). Disruptions to genome organization are frequently seen in human diseases, including cancer (15, 16), where improper chromosome folding allows promoters to hijack regulatory sequences for inappropriate expression (17, 18). Given the requirement for cells to correctly organize DNA to ensure genome function, there is a critical need to understand how this genome organization occurs, including the factors required to correctly fold the genome in wild type (WT) nuclei.

Eukaryotic organisms from fungi and yeasts to metazoans hierarchically organize their genomes in the nucleus (19). At the most basic level, a histone octamer wraps ~146 basepairs (bp) of DNA to form nucleosomes (20–22), which are compacted into chromatin fibers. In higher eukaryotes, including humans, the cohesin protein complex then extrudes chromatin fibers to form globules or loops across a chromosome, with a CTCF dimer anchoring the loop base (23–30). Metazoan loops are further compacted into Topologically Associated Domains (TADs, also called “contact domains”), where chromatin internal to the TAD is more apt to interact than external chromatin (31–35). TADs containing chromatin of similar transcriptional states are compartmentalized, while individual chromosomes isolate into territories (32, 36–38). The genomes of more simplistic organisms, such as the filamentous fungal model organism *Neurospora*

crassa, are also hierarchically organized and are similarly compacted as metazoan genomes. For example, Neurospora has a nearly identical ratio of genome size to nuclear volume as humans, and Neurospora chromosomes form TAD-like structures, initially termed "Regional Globule Clusters", comprised of several (presumably cohesin-dependent) chromatin loops (39–42). Flanking heterochromatic regions strongly interact to delineate Neurospora TAD-like structures, which promotes multiple euchromatic globules to associate in an uninsulated manner (39, 41). As opposed to the chromosome territories seen in metazoans (2, 36, 43, 44), the vast majority of fungal chromosomes are in a Rabl conformation, in which centromeres bundle at distinct sites from the telomere clusters on the inner nuclear membrane (19, 40, 42, 45, 46). The Rabl chromosome conformation has been directly observed in *Neurospora crassa*, with discrete centromeric and telomeric foci associated with the inner nuclear membrane (41, 47, 48).

Despite the marginal chromosome conformation differences between fungi and metazoans, filamentous fungi like *Neurospora crassa* remain excellent model organisms to understand the underlying mechanisms driving eukaryotic genome organization (39, 41, 48). The predominantly haploid genomes of fungi are small (e.g., the Neurospora genome is 4.1×10^7 bp) (49, 50), making fungi cost-efficient for genomic experiments. The composition of the Neurospora genome mirrors that of humans, as its genome is separated into euchromatic and heterochromatic regions, the latter being subdivided into the permanently silent constitutive heterochromatin covering the AT-rich and repetitive DNA that is devoid of genes, and the temporarily silent facultative heterochromatin that covers gene rich regions for transcriptional repression during asexual growth (49–53). Similar to metazoans, Neurospora employs post-translational modifications (PTMs) of histone proteins and covalent modifications of DNA for differentiating heterochromatin from euchromatin; these modifications are necessary for numerous genomic processes, including the regulation of gene expression. Neurospora constitutive heterochromatin is enriched with trimethylation of lysine 9 on histone H3 (H3K9me3) and cytosine methylation (5^mC), while facultative heterochromatic regions are enriched with di- or trimethylation of lysine 27 on histone H3 (H3K27me2/3) or the ASH1-dependent dimethylation of lysine 36 on histone H3 (H3K36me2) (51–58). Euchromatic regions are enriched with di- or trimethylation of lysine 4 on histone H3 (H3K4me2/3) or acetylation of lysine residues, including lysine 9 on histone H3 (H3K9ac) or lysine 16 on histone H4 (H4K16ac) (59–62). However, in contrast to metazoans,

the machinery that catalyze histone PTMs or 5^{m}C is often simplistic, non-redundant, and not required for viability, allowing researchers to dissect individual modification pathways (53, 63–65). Taken together, the advantages offered by filamentous fungi such as *Neurospora crassa* strongly argue that filamentous fungal systems are useful for studying the role of histone or DNA modifications in organizing eukaryotic genomes.

One method to assess genome organization is chromosome conformation capture coupled with high throughput sequencing (Hi-C), in which chromatin is crosslinked, digested with restriction enzymes, and ligated, thereby physically connecting DNA that is interacting into a single DNA molecule (66); Hi-C allows researchers to capture and examine the interactions between loci across the entire genome of an organism (38). Advances in Hi-C protocols enable the capture of DNA ligation products in the nucleus, such that these *in situ* Hi-C datasets more accurately capture interacting chromatin (32). This has enabled researchers to characterize genome organization at high resolutions with unprecedented clarity (32, 39). Hi-C has elucidated or confirmed the foundations of hierarchical genome organization in eukaryotic nuclei, including globules, TADs, and chromosome territories (or the Rabl chromosome conformation, if fungal systems are examined) (19, 31, 32, 36, 39–41, 44). However, the underlying mechanisms driving genome organization in any species are currently unknown.

Arguably, one critical yet understudied genome component that may drive chromosome conformation in WT nuclei through genome compartmentalization are histone PTMs. Specific histone PTMs define the transcriptional status and chromatin accessibility in the nucleus (22, 67–69). Since euchromatic regions associate but are segregated from heterochromatic clusters, the possibility exists that the histone PTMs defining each chromatin type could impact genome topology. Recent reports detail how histone PTMs, as well as the effector proteins that bind these marks, have critical roles in genome organization. Notably, the constitutive heterochromatin-specific H3K9me3 mark and its cognate binding partner Heterochromatin Protein-1 (HP1) are important for pericentromeric region association during zygote genome activation in Drosophila and the compaction of heterochromatic regions during fungal asexual growth (41, 70). In addition, sub-telomeric H3K27me2/3, which demarcates facultative heterochromatin, is necessary for telomere clusters to associate with the nuclear periphery in Neurospora (48). These results suggest that heterochromatic histone PTMs play vital roles in eukaryotic genome organization. However, there is scant

information about the role of other histone PTMs, including histone acetylation.

The addition of an acetyl group to histones has long been thought necessary for opening chromatin, as enrichment of acetylation in euchromatic regions is readily observed in fungi, fruit flies, mice, and humans (54, 71–80). In contrast, heterochromatic regions are typically devoid of histone acetylation, which occurs due to the action of histone deacetylase (HDAC) complexes (54, 59, 60, 81). Recent results have argued that changes in chromatin acetylation levels can impact genome organization. For example, as human epidermal cells differentiate, numerous enhancers gain acetylation of lysine 27 on histone H3 (H3K27ac) and form novel interactions with promoters controlling epidermis differentiation (82). A similar gain of H3K27ac, which may be dependent on the p300 histone acetyltransferase, forms novel promoter-enhancer contacts for inducing transcription during the differentiation of mouse adipocyte cells (83). Mitotic cell cycle stage entry depends on histone acetylation changes during human and mouse cell cycles. In general, mitotic chromosomes are globally hypoacetylated, which creates dense chromosome structures for homologous chromosome separation into daughter cells (84–88); the HDAC Hst2p in *S. cerevisiae* is important for deacetylating H4K16 for chromosome condensation (86). As cells transition through mitosis, promoters and enhancers specifically lose H3K27ac, but rapidly regain this mark in G1 for reactivating gene transcription and reforming TADs (89, 90). Further, improper recruitment of P300 by a novel oncogenic protein, BRD4-NUT, which translationally fuses the acetylated histone-binding bromodomain of BRD4 to the P300-binding C-terminus of NUT (Nuclear protein in testis), creates hyperacetylated Megadomains that aggregate into a subcompartment characterized by increased transcription activation (91). Hyperacetylated chromatin in the presence of bromodomain proteins may actually form a novel phase-separated state that could promote the formation of nuclear subcompartments (92). Together, these data implicate histone acetylation as having a critical role in the organization and function of eukaryotic genomes. However, few studies assess the action of HDAC complexes on fungal chromosome conformation.

Neurospora crassa is excellent for studying histone deacetylase (HDAC) action, as it encodes four class II HDACs (HDA-1 to HDA-4; class II characterization based on primary structure conservation) (81), each of which may be targeted to different chromatin types (62). Specifically, HDA-1 is the Neurospora HDAC that impacts heterochromatin, as a Δ*hda-1* deletion strain loses $5^{m}C$ (62, 93). HDA-1 is a component of the four-

member HCHC complex, comprised of the proteins HDA-1, CDP-2 (***C***hromo***d***omain ***P***rotein-***2***), HP1, and CHAP (***C***DP-2 and ***H***DA-1 ***A***ssociated ***P***rotein) (59, 60). Within the HCHC complex, HDA-1 is the deacetylase catalytic subunit, HP1 binds to H3K9me3 for heterochromatin recruitment, and CDP-2 and CHAP are required for protein interactions within the HCHC and binding to AT-rich DNA, respectively (59, 60). The N-terminus of CDP-2 forms critical protein-protein interactions with HDA-1 within the HCHC complex, and while the CDP-2 chromodomain can also bind H3K9me3, this domain is dispensable for HCHC function (60). CHAP also forms protein-protein interactions with HDA-1, but its primary structure also contains two AT hook domains that allow the HCHC complex to associate with the AT-rich DNA of constitutive heterochromatin (59, 60). Both CDP-2 and CHAP are necessary for HDA-1 to localize to heterochromatic genomic loci, and HDA-1-dependent deacetylation is necessary for H3K9me3 deposition (59, 94). Importantly, strains deleted of *cdp-2*, *chap*, or *hda-1* have increased histone acetylation and have decreased H3K9me3 at select heterochromatic regions, including the centromeres, as assessed by Chromatin Immunoprecipitation quantitative PCR, although it is unknown if these enrichment changes occur genome-wide (60). HCHC mutant strains also have changes in 5^{m}C: smaller heterochromatic regions lose 5^{m}C but larger regions, including the centromeres, gain 5^{m}C by increasing recruitment of DIM-2, the only DNA methyltransferase encoded in Neurospora (59). Given the extensive background information available for HCHC complex action, strains devoid of HCHC members provide an outstanding system to explore the role of epigenetic marks on eukaryotic genome organization.

Here, we report the changes to the genome organization in Δ*cdp-2* or Δ*chap* deletion strains, as assayed by euchromatin-specific (*Dpn*II) or heterochromatin-specific (*Mse*I) *in situ* Hi-C (39). We reasoned that these HCHC members might impact the formation of higher order structures in genome organization in addition to their reported roles for HDA-1 recruitment. We found that the loss of CDP-2 causes increased interactions between distant heterochromatic regions on a single chromosome and between chromosomes consistent with increased accessibility of silent chromatin. In contrast, loss of CHAP reduces the local compaction of heterochromatic regions to indirectly increase regional euchromatic contacts. Across the genome of a Δ*cdp-2* strain, heterochromatic regions gain enrichment of acetylation of lysine 16 on histone H4 (H4K16ac) but not acetylation of lysine 9 on histone H3 (H3K9ac), as assessed by Chromatin Immunoprecipitation-

Sequencing (ChIP-seq); a Δ*chap* strain has few H4K16 acetylation changes. Surprisingly, a subset of heterochromatic regions in a Δ*cdp-2* strain lose H3K9me3, resulting in increased heterochromatic region contact promiscuity. Moreover, a Δ*cdp-2*;Δ*dim-2* double mutant, which is devoid of $5^{m}C$ in an HCHC-deficient background, gains H3K9me3 at most AT-rich regions and has a highly disordered genome organization, with increased contact probabilities between heterochromatic loci and euchromatin, which implies silent chromatin no longer associates in a heterochromatic bundle at the nuclear periphery. Our results suggest that histone deacetylation is necessary for proper genome topology, while in the presence of hyperacetylated histones, cytosine methylation increases maintain the segregation of heterochromatin from euchromatin.

Results

Genome organization changes in strains deleted of either HCHC component CDP-2 or CHAP

Recent analysis of genome organization in the filamentous fungal model organism *Neurospora crassa* has shown that the seven chromosomes of the wild type (WT) strain N150 (74-OR23-IVA [FGSC #2489]) are organized in a Rabl structure defined by independent centromere and telomere clusters at the nuclear periphery (39, 41, 48). In the Rabl conformation, the arms of each Neurospora chromosome strongly associate (Figure 1A), while extensive inter-chromosomal contacts – and weak chromosome territories – are readily visible (39, 41, 47). Also, chromatin is segregated: silent heterochromatic regions strongly interact across Megabases (Mb) of linear chromosomal distance, or between chromosomes, to form aggregates at the nuclear periphery, while active euchromatic regions are hierarchically compacted into loops/globules that form TAD-like structures in the center of the nucleus (Figure 1A) (19, 39). These interaction characteristics of Neurospora chromatin were elucidated by chromatin-specific Hi-C, where the use of the restriction enzyme *Mse*I (recognition sequence T^TAA) primarily assesses contacts in the AT-rich heterochromatic regions of the Neurospora genome, while GC-rich euchromatic region contacts are examined with *Dpn*II (^GATC) (Figure 1A) (39). Despite these advances, little is known about how changes in histone PTMs, such as the removal of histone acetylation by histone deacetylases (HDACs), impact eukaryotic genome organization. Since AT-rich, silent genomic regions are important for fungal chromosome conformation, we examined if the loss of the heterochromatin specific HDAC complex HCHC could impact genome organization.

To understand how dysfunction of the HCHC histone deacetylase complex can impact fungal genome organization, we examined strains independently deleted of the genes encoding CDP-2 (Δ*cdp-2*) or CHAP (Δ*chap*) using Hi-C. Since CDP-2 and CHAP recruit HDA-1 to AT-rich genomic loci for the deacetylation of histones, the activity of CDP-2 and CHAP could be epistatic to HDA-1 action, yet given the unique domains predicted from their primary structures, these proteins could have distinct functions in the HCHC complex (59, 60). We hypothesized that by examining mutants of CDP-2 and CHAP, we could assess how compromised HCHC function alters chromosome conformation while possibly observing more nuanced differences in genome organization, which would clarify the individual roles of these HCHC members, rather than only examining the effect of deleting the HDA-1 catalytic subunit. Therefore, we independently performed *in situ* Hi-C with *Dpn*II to assess primarily euchromatic contacts, or *Mse*I to examine mainly heterochromatic interactions, on Δ*cdp-2* and Δ*chap* strains. Our replicate *in situ* Hi-C libraries for these strains were highly reproducible (Figures S1, S2), allowing us to merge the datasets generated with similar restriction enzymes. This produced high quality *Dpn*II Δ*cdp-2* (~35.4 million [M] valid read pairs) and Δ*chap* (~8.7M valid read pairs), as well as *Mse*I Δ*cdp-2* (~13.9M valid read pairs) and Δ*chap* (~4.8M valid read pairs) datasets; total and valid read counts are provided in Supplemental Table S1. The merged *Dpn*II datasets presented here are Knight-Ruiz (KR) corrected to limit any experimental bias (36, 95, 96), while *Mse*I datasets in all figures display raw, uncorrected contact probabilities, since KR correction improperly removes specific interactions between heterochromatic regions upon bin averaging, possibly caused by the discrepancy between the number of *Mse*I sites in AT-rich heterochromatic regions and more GC-rich euchromatin (39).

At first glance, when examining a single chromosome (Linkage Group [LG] II), the *Dpn*II and *Mse*I Δ*cdp-2* datasets (Figures 1B) look comparable to WT *Dpn*II or *Mse*I Hi-C datasets (Figure 1A) generated from fastq files containing nearly identical numbers of valid reads. However, at a closer look, the Δ*cdp-2* dataset has increased interactions between distant heterochromatic regions, including the LG II centromere interacting more strongly with heterochromatic regions up to three megabases (Mb) distant, which were the most evident in the silent chromatin-specific *Mse*I heatmap (Figures 1B, black arrowheads); also, heterochromatic regions form fewer contacts with nearby euchromatin (Figure 1B, open arrowheads), as contacts between heterochromatic regions are more prevalent. These effects are seen on all Neurospora chromosomes

(Figures S3). To more easily highlight changes in a Δ*cdp-2* strain, we compared the *Dpn*II or *Mse*I Hi-C contact maps between WT and the Δ*cdp-2* strain. In both datasets, the most prominent change in LG II interactions are the strong increases between centromeres and distant heterochromatic regions, evident as strong red bins in the comparison heatmaps (Figure 1C); a similar pattern of increased interactions between heterochromatic regions is observed on all seven Neurospora LGs (Figures S4). Further examination of the changes in centromeric contacts at a higher resolution show how centromeric chromatin is more likely to form interactions, as the LG II centromere has a strong red diagonal indicative of increased contacts between centromeric nucleosomes, as well as more intense interactions with distant H3K9me3-marked constitutive heterochromatic regions (Figure 1D). In fact, each heterochromatic region across LG II has increased local interactions along the diagonal of Δ*cdp-2 MseI* datasets relative to WT, arguing this AT-rich, heterochromatic DNA associates less with its own histone proteins, which would allow greater contact promiscuity with the AT-rich DNA of nearby heterochromatic nucleosomes; this could additionally deplete heterochromatic-euchromatic contacts when equal numbers of valid Hi-C read pairs are compared (Figures 1B, open arrowheads, 1C). Quantification of strongly changed contacts between WT and Δ*cdp-2 Mse*I datasets showed that, indeed, the greatest number of strongly increased contacts occurred between H3K9me3-enriched bins; few contacts were strongly increased between H3K9me3 enriched bins and bins enriched with euchromatic marks (Figure 1H). Further, as assessed in euchromatin-specific *Dpn*II datasets, interactions of more distant euchromatic regions were also decreased, such that interactions between the left and right chromosome arms, as well as the interactions between distant TAD-like structures were reduced (Figure 1C). The strong decrease in interactions just off diagonal when comparing the WT and Δ*cdp-2 Mse*I datasets (Figure 1C, above diagonal) could also indicate chromatin in TAD-like structures interact less, similar to the changes in *Dpn*II Δ*cdp-2* datasets, but equally possible is that these decreased euchromatic contacts reflect the paucity of contacts due to the reduced number of *Mse*I sites in euchromatin (39) coupled with the increased numbers of heterochromatin-specific contacts within these datasets (Figure 1C). All told, the loss of CDP-2 in Neurospora causes increased constitutive heterochromatic region interactions and decreased associations between euchromatin.

To further understand the function of HCHC components, we examined the genome organization of a

Δ*chap* strain by *Dpn*II and *Mse*I Hi-C. We note that both of these datasets have reduced numbers of valid reads compared to the data from a Δ*cdp-2* strain, with the Δ*chap Dpn*II Hi-C having ~four-fold less reads and the Δ*chap Mse*I Hi-C having ~three-fold less valid reads (Supplemental Table S1). However, despite these differences in valid read numbers, we believe that there is enough information present to assess the impact of CHAP loss, especially considering that we, again, normalized the WT datasets with similar numbers of valid reads to highlight differences from normal genome topology. Examination of single chromosomes show how the Δ*chap Dpn*II and *Mse*I Hi-C datasets appear devoid of most strong long-range contacts (Figures 1E); similar results were shown for all seven Linkage Groups (Figure S5). In each chromosome, more distant contacts are rarer upon CHAP loss; an enhanced image of the right arm of LG II highlights that regional interactions still form in both *Dpn*II and *Mse*I datasets (Figure 1E). When equal numbers of valid reads between the WT and Δ*chap* datasets are compared, the differences from the normal genome organization are readily apparent, with heterochromatic regions exhibiting reduced internal compaction and reduced contacts between heterochromatic regions across LG II (Figures 1F-G, arrowheads); similar differences occur on each chromosome upon CHAP loss (Figure S6). Also apparent are the decreased interactions between the TAD-like Regional Globule Clusters (RGCs) (39) in the Δ*chap Dpn*II data, which may stem from the slight increase in on-diagonal, local interactions. Highlighting these genomic organization changes, quantification of strongly increased contacts between bins enriched for either activating or repressive histone PTMs, including the SET-2-specific H3K36me2 or H3K27ac (54), shows minimal gains in bin interactions between heterochromatic and euchromatic bins, yet euchromatic regions are more likely to contact in a Δ*chap* strain (Figure 1H), perhaps indirectly resulting from decreased heterochromatic compaction reducing the numbers of strong contacts between heterochromatic bins.

Our data suggest that CDP-2 and CHAP have different functions in genome organization. Highlighting the differences between these two strains, we compared equal numbers of valid Hi-C reads from Δ*cdp-2* and Δ*chap* datasets. Figure 1I shows how genome topology is changed in a Δ*chap* strain relative to that in Δ*cdp-2*. In a Δ*chap* strain, the decrease in heterochromatic region compaction and contacts between silent regions, with the concomitant increase in euchromatic interactions, is evident (Figure 1I, arrowheads). These data argue that CHAP is necessary for forming intra-chromosomal interactions within and between

heterochromatic regions, while CDP-2 may be indirectly acting to restrict heterochromatin aggregation, given its role in controlling histone acetylation (below). Highlighting this functional difference are the centromeres, which are among the genomic loci gaining the most $5^{m}C$ in Δ*cdp-2* and Δ*chap* strains (59, 60). Upon closer inspection of the centromere topology in *Mse*I datasets, the Δ*cdp-2* strain shows a strong increase in local contacts ~one to two 10kb bins off diagonal with subtle increases between the more distant centromeric chromatin, suggesting that the DNA wrapped around individual centromeric nucleosomes can contact more-distant nucleosomes rather than being restricted to interactions with nucleosomes in close proximity within centromeric chromatin fibers (Figure 1J). In contrast, Δ*chap Mse*I data has reduced interactions between more distant nucleosomes in centromeric chromatin, implying that CHAP acts to stabilize the folding and compaction of the centromeric chromatin (Figure 1J).

Similar interaction trends are observed with the heterochromatic interactions between chromosomes, arguing that CDP-2 and CHAP facilitate the global clustering of heterochromatic regions in the Neurospora nucleus. As shown in raw *Mse*I and KR corrected *Dpn*II Hi-C data from a Δ*cdp-2* strain, or when these Δ*cdp-2* data are compared to WT Hi-C, the centromeres in a Δ*cdp-2* strain gain interactions with the interspersed heterochromatic regions across all seven LGs; the gain in heterochromatic region interactions may reduce contact strength of the euchromatin surrounding the centromere of each chromosome, as well as the inter-chromosomal centromeric interactions (Figures 2A, S7), although it is possible this reduction manifests when equal numbers of valid read pairs are compared between datasets where one (Δ*cdp-2*) has more heterochromatin contacts. Specifically, the *Dpn*II Hi-C data present stronger inter-chromosomal contacts, especially between chromosome arms (Figures 2A, S7), which may occur when heterochromatic regions between chromosomes are more apt to interact; similar changes to centromere interactions are observed in KR-corrected *Mse*I data and raw *Dpn*II data when WT and Δ*cdp-2* contact matrices are compared (Figure S8, top). Examination of the interactions between two chromosomes, LG II and LG III, in Δ*cdp-2 Mse*I Hi-C contact heatmaps show the expansion of centromeric and interspersed heterochromatic region contacts and the concomitant reduction of contacts between silent and active chromatin (Figure 2B). Plotting the inter-chromosomal interaction changes between WT and Δ*cdp-2 Mse*I datasets highlight the strong contact gain between heterochromatic regions on different chromosomes, including how the centromeres on LG II and

LG III more readily contact distant heterochromatic regions rather than form inter-centromeric contacts, which are moderately decreased, as is the euchromatin emanating from the LG II and LG III centromeres (Figure 2C). In contrast, the loss of CHAP reduces heterochromatic interactions across the Neurospora genome: as shown in Δ*chap Mse*I contact matrices (Figure S9), or when Δ*chap Mse*I data is compared to WT *Mse*I data (Figure 2D), few inter-chromosomal heterochromatic contacts are observed, with the reduction in centromeric contacts being the most prominent; these differences in contact strength are independent of matrix correction (Figure S8, bottom). In fact, the comparison of Δ*cdp-2* and Δ*chap* contact matrices shows how inter-chromosomal centromeric contacts are stronger in a Δ*cdp-2* strain (Figure S10). A plot of the interactions between two chromosomes, LG II and LG III, in Δ*chap* highlights the paucity of constitutive heterochromatic contacts between chromosomes (Figure 2E), which is further evident when *Mse*I Hi-C data between a WT and Δ*chap* strain are compared (Figure 2F). This decrease in heterochromatic bundling compromises the inter-chromosome arm interactions that are characteristic of the Rabl conformation (19, 97), as the comparison of *Dpn*II Hi-C between WT and Δ*chap* strains shows reduced euchromatin interactions across the left and right arms of each Neurospora Linkage Group (Figure 2D). Quantification of the strongest gains in inter-chromosomal interactions between WT and these HCHC deletion mutants confirm these genome topology changes. Specifically, in Δ*cdp-2 Mse*I Hi-C datasets, 81.5% of H3K9me3-enriched bins have strong contact gains, while few H3K9me3 enriched bins have strong interaction changes with bins marked by euchromatic histone PTMs (Figure 2G, left panel). The Δ*cdp-2 Dpn*II Hi-C data only show strong gains between euchromatic bins enriched with H3K27ac and SET-2 specific H3K36me2 (Figure 2G, right panel). In contrast, Δ*chap Mse*I and *Dpn*II Hi-C datasets have minimal contact increases relative to WT independent of histone PTMs, indicating the loss of CHAP reduces the chromosomal compaction across the Neurospora genome (Figure 2G). All told, our Δ*cdp-2* and Δ*chap* Hi-C data reveals the differential effects on genome organization by individual members of a histone deacetylase complex.

Histone acetylation changes in single deletion strains of the HCHC components CDP-2 and CHAP

Our Hi-C analysis suggests that single deletion strains of the genes encoding the HCHC members CDP-2 and CHAP uniquely impact the Neurospora chromosome conformation. To understand how altered HCHC

function can affect the folding of DNA in the fungal nucleus, we decided to correlate changes in genome topology to levels of histone acetylation enrichment in these strains. However, no genome-wide Chromatin Immunoprecipitation (ChIP) sequencing (ChIP-seq) datasets of HCHC mutants are publicly available to make this assessment; recent work showing histone acetylation changes in Δ*cdp-2* and Δ*chap* strains only used ChIP qPCR to show that loss of CDP-2 and CHAP generally increases histone acetylation levels at several heterochromatic loci (60), precluding genome-wide conclusions or correlation to genome organization. Therefore, we performed two ChIP-seq replicates on the levels of histone acetylation on two lysine residues, K9 on histone H3 (H3K9ac) and K16 on histone H4 (H4K16ac), in Δ*cdp-2*and WT strains, and we performed H4K16ac ChIP-seq on a Δ*chap* strain. Both H3K9ac and H4K16ac were proposed to be targets of the HCHC complex, as assessed by ChIP qPCR (60). Our H3K9ac and H4K16ac ChIP-seq replicates are qualitatively reproducible in each strain (Figure S11, S12), so we merged the replicates of each PTM into two fastq files that independently present the data for H3K9ac or H4K16ac for display on the Integrative Genome Viewer (IGV) (98); all ChIP-seq data here has been normalized using Reads Per Kilobase per Million reads (RPKM) to ensure proper comparison between each experiment, although we do acknowledge that the use of spike-in DNA samples could have detected additional enrichment changes (99–101). Consistent with the published qPCR ChIP, CDP-2 loss caused an increase in H4K16ac enrichment only in AT-rich heterochromatic regions but had little effect on the levels of H3K9ac regardless of location (Figure 3A, top). Zooming into the right arm of LG II highlights the changes in H4K16ac, as each H3K9me3-marked heterochromatic region has an increase in H4K16ac relative to WT, but H3K9ac was not enriched (Figure 3A, bottom, arrowheads). Little change in the enrichment of either H4K16ac or H3K9ac in a Δ*cdp-2* strain in the flanking euchromatic regions was observed (Figure 3A), highlighting the specificity of the HCHC complex for deacetylating only AT-rich heterochromatic regions in the Neurospora genome. The lack of H3K9ac enrichment in heterochromatin may reflect the H3K9 tri-methylation levels in these gene-poor regions (Figure 3A, dark green track). In contrast to the increase in H4K16ac in a Δ*cdp-2* strain, the loss of CHAP had little effect on acetylation: the Δ*chap* strain showed minimal, if any, changes to the enrichment of H4K16ac across genes and within constitutive heterochromatic regions (Figure S13A).

These acetylation changes are highlighted by plots and heatmaps of the average enrichment for the

RPKM-normalized H4K16ac and H3K9ac datasets across either H3K9me3-enriched regions or genes. When all constitutive heterochromatic regions are scaled to 10 kilobases (kb) in length, the gain of H4K16ac is readily apparent, as essentially all AT-rich regions have a substantial increase in H4K16ac enrichment in a Δ*cdp-2* strain relative to a WT strain in which constitutive heterochromatic regions are normally devoid of H4K16ac and the flanking regions are highly acetylated (Figure 3B). In contrast, the enrichment of H3K9ac in the heterochromatic regions of a Δ*cdp-2* strain is non-existent, and in fact may be lower than a WT strain (Figure S14A), possibly due to the H3K9me3 enrichment in constitutive heterochromatic regions. Similarly, a Δ*chap* strain has only subtle increases in H4K16ac across constitutive heterochromatin, and no change in genic H4K16ac (Figure S13B-C), highlighting the specific differences on acetylation activity of HCHC components. When genes are scaled to 2.5 kb, only a small reduction in H4K16 acetylation is seen in a Δ*cdp-2* strain compared to the WT strain. The possibility exists that the increased acetylation of heterochromatic nucleosomes by histone acetyltransferases interferes with the normal acetylation of genes in euchromatic regions; the deposition of H3K9ac in genes may have a subtle shift in distribution away from the 5' end of genes in a Δ*cdp-2* strain (Figure S14B). To further characterize the H4K16ac and H3K9ac deposition changes, we plotted the normalized, averaged signal of each region used in average enrichment heatmaps on boxplots to show how the average signal in each region is changed. Here, the Δ*cdp-2* constitutive heterochromatic regions have robust changes in H4K16ac signal relative to WT (Figure 3D), while H3K9ac enrichment is overall decreased (Figure S14C), although some regions in each dataset go against these trends. Considering euchromatic acetylation, a Δ*cdp-2* strain has small but statistically significant changes: H4K16ac is decreased over genes (Figure 3E) while genic H3K9ac is increased (Figure S14D). Together, we conclude that loss of HCHC activity has differential effects on lysine residues in histone proteins, with deletion of the gene encoding CDP-2 having the strongest effect on H4K16ac, while the loss of CHAP minimally affects histone acetylation enrichment.

Changes in H3K9me3-deposition and heterochromatin bundling in Δcdp-2 *and* Δchap *strains*

Given the changes to acetylation in constitutive heterochromatic regions in strains with compromised HCHC function, we decided to assess H3K9me3 enrichment by ChIP-seq to examine whether Δ*cdp-2* and

Δ*chap* strains exhibit differences in their permanently silent genomic loci. The H3K9me3 ChIP-seq replicates of each strain are reproducible, allowing us to merge the two replicates from each strain into single, merged fastq files (Figure S15). Levels of H3K9me3 enrichment in a Δ*cdp-2* strain resemble that of a WT strain: most regions appear to have similar levels of H3K9me3 deposition (Figure 4A). However, at closer examination, several moderately sized constitutive heterochromatic regions have a near-complete or total loss of H3K9me3 (Figure 4A, arrowheads), while other nearby constitutive heterochromatic regions still retain normal H3K9me3 levels (Figure 4A). Zooming into one affected region, we observe background levels of H3K9me3 across that entire locus, suggesting the underlying DNA is unchanged in regions losing H3K9me3, allowing for normal ChIP-seq read mapping (Figure 4A, red box). In contrast, the loss of CHAP causes minimal H3K9me3 loss, and in fact, most heterochromatic regions have increased enrichment of H3K9me3 signal relative to WT, even with RPKM normalized ChIP-seq tracks (Figure S13A).

Examination of H3K9me3-marked loci in the Neurospora genome using average enrichment plots and heatmaps highlight the changes in constitutive heterochromatic regions in Δ*cdp-2* and Δ*chap* strains. Most heterochromatic regions, but not genes, gain H3K9me3 enrichment with loss of CHAP (Figure S13D-E). Conversely, while many heterochromatic regions are unchanged with the loss of CDP-2, a substantial number of silent loci have reductions, or completely lose, H3K9me3 (Figure 4B). Boxplots of average signal across heterochromatic regions highlight this change, with the majority of AT-rich regions losing H3K9me3 signal in a Δ*cdp-2* strain (Figure 4C). We were curious as to how the loss of H3K9me3 and gain of H4K16ac might affect the genome organization of these formerly heterochromatic regions. Plotting the changes in contact probability between WT and Δ*cdp-2* Hi-C across two regions on LG III and LG I, each of which encompass AT-rich regions losing H3K9me3 in a Δ*cdp-2* strain, shows how the changes in histone PTMs affected long-range heterochromatic bundling (Figure 4D). In both instances, regions losing H3K9me3 have strong increases in interactions with other AT rich regions retaining this silencing mark. For example, on LG III, the contacts between two nearby AT-rich genomic regions are increased when one region loses H3K9me3, while two other, similarly sized heterochromatic regions have few changes in long-range interactions (Figure 4D, top panel, compare the closed and open arrowheads). Also, on LG I, the loss of H3K9me3 from (and concomitant gain of H4K16ac in) multiple regions caused gains in inter-region contacts; other nearby regions that retain

H3K9me3 are unaffected (Figure 4D, bottom panel, closed arrowheads). All told, the deletion of the gene encoding CDP-2 causes changes in the enrichment of histone PTMs that cause the typically heterochromatic AT-rich genomic loci to form a more open chromatin structure, which increases the likelihood of these regions contacting other heterochromatic regions in the silent chromatin bundle.

Changes in histone PTMs and genome organization in a Δcdp-2;Δdim-2 *double mutant*

Our work to this point has characterized the unique changes in genome organization and histone post-translational modifications of strains individually deleted of a member of the histone deacetylase complex HCHC. These changes primarily affect heterochromatic regions, as the gain in histone acetylation can affects the deposition of H3K9me3 and the bundling of silent chromatin. However, loss of CDP-2 or CHAP also alters the deposition of cytosine methylation: the centromeres and other longer interspersed heterochromatic regions gain $5^{m}C$, while some shorter AT-rich regions lose $5^{m}C$ enrichment in Δ*cdp-2* and Δ*chap* strains (59, 60). Hypothetically, extra $5^{m}C$ in the heterochromatin of a Δ*cdp-2* strain may confer additional properties to these AT-rich regions, meaning the cytosine methylation gains must be considered when assessing genome organization. In support, $5^{m}C$ must be important when the HCHC is compromised, given that the Δ*cdp-2*;Δ*dim-2* strain, deleted of the gene DIM-2, which is the single DNA methyltransferase in Neurospora, has a compromised growth rate relative to single HCHC mutants (60).

To fully understand if this $5^{m}C$ increase can alter histone PTM deposition following HCHC complex loss, we examined levels of H4K16ac and H3K9me3 using ChIP-seq. Replicates of these ChIP-seq experiments are qualitatively comparable (Figures S12, S15), allowing us to merge ChIP-seq replicates of identical histone PTMs; as before, all ChIP-seq datasets are normalized by RPKM. Compared to a Δ*cdp-2* strain, H4K16ac distribution in a Δ*cdp-2*;Δ*dim-2* strain is essentially unchanged (Figure 5A-B, blue tracks), where both strains had an increase in heterochromatic acetylation and minimal changes to genic acetylation in euchromatin (Figure 5A-B), suggesting that DIM-2 loss minimally impacts acetylation of AT-rich DNA. Quantification of the normalized average H4K16ac enrichment across heterochromatic regions in a Δ*cdp-2*;Δ*dim-2* double mutant is slightly reduced relative to the Δ*cdp-2* single mutant but still strongly increased when compared to WT H4K16ac enrichment (Figure 5C). Regarding H3K9me3, most AT-rich regions in a Δ*cdp-2*;Δ*dim-2*

455 strain strongly gain this silencing mark relative to WT and Δ*cdp-2* strains (Figure 5A, 5D). However, the same
456 ~20% of AT-rich regions that completely lack H3K9me3 in a Δ*cdp-2* strain are also devoid of H3K9me3 in
457 the double mutant (Figures 5A, asterisks; 5D), suggesting the underlying DNA sequence of these AT-rich
458 regions occlude H3K9me3 deposition. Quantification of the averaged H3K9me3 enrichment of these AT-rich
459 regions highlights the substantial increase in H3K9me3 signal in a Δ*cdp-2*;Δ*dim-2* double mutant (Figure 5E).
460 Thus, histone acetylation gains coupled with 5^{m}C loss at AT-rich regions can signal for increased H3K9me3
461 by the DIM-5 catalytic subunit of the DCDC, the H3K9 methyltransferase complex in Neurospora (65).

462 To assess if additional heterochromatic acetylation coupled with 5^{m}C loss impacts genome organization,
463 we performed *in situ* Hi-C on the Δ*cdp-2*;Δ*dim-2* strain using *Dpn*II. We chose to use only *Dpn*II to assess
464 contact changes in euchromatin for a general assessment of the genome organization. We generated two *in*
465 *situ Dpn*II Hi-C replicates of a Δ*cdp-2*;Δ*dim-2* strain which are highly correlated (Figure S16), allowing us to
466 merge the replicates into a single *Dpn*II Δ*cdp-2*;Δ*dim-2* Hi-C dataset that contained 23.1M valid read pairs
467 (Table S1). The contact frequency heatmap for the Δ*cdp-2*;Δ*dim-2* strain shows the typical segregation of
468 heterochromatic regions from euchromatin typical for *Dpn*II datasets, as observed in a single chromosome
469 (LG II; Figure 6A top), all other Neurospora LGs (Figure S17), or across the entire Neurospora genome (Figure
470 S18A). A KR corrected (reduced bias) contact probability heatmap of the entire Δ*cdp-2*;Δ*dim-2* genome or
471 only LG II shows the centromeric bundling independent of telomere clusters typical of the Rabl conformation
472 (Figures 6A, bottom, S18B), indicating that the overall genome organization of the Δ*cdp-2*;Δ*dim-2* strain is
473 maintained.

474 However, comparison of equal numbers of valid read pairs of the Δ*cdp-2*;Δ*dim-2 Dpn*II Hi-C dataset to a
475 WT *Dpn*II dataset showed strong changes in genome organization of the double mutant, with Δ*cdp-2*;Δ*dim-2*
476 heterochromatic regions interacting more with surrounding euchromatin. Both raw and KR corrected
477 heatmaps comparing the WT and Δ*cdp-2*;Δ*dim-2* contact probabilities show that AT-rich heterochromatic
478 regions, including the centromere, gain interactions with the flanking gene-rich euchromatic DNA (Figure
479 6B). Notably, the increased interactions between heterochromatic regions evident upon CDP-2 loss (e.g.,
480 Figures 1B-D) do not occur in a Δ*cdp-2*;Δ*dim-2* strain, suggesting that heterochromatin can cluster, as in WT,
481 but the inter-heterochromatic contact gains are abrogated by 5^{m}C loss. In addition, obvious reductions in

local and regional euchromatic interactions are observed (Figure 6B), suggesting normal genic contacts are less likely to form and possibly explaining the growth deficiency of the Δ*cdp-2*;Δ*dim-2* strain. Quantification of the strongly changed intra-chromosomal interactions in the Δ*cdp-2*;Δ*dim-2* dataset relative to the WT dataset show more H3K9me3 enriched bins as gaining contacts, often to bins enriched for euchromatic histone PTMs; greater numbers of bins enriched for euchromatic marks also strongly gain contacts in the double mutant (Figure 6C). These contact probability changes are not isolated to LG II, as the other chromosomes, as well as the whole genome, present with similar contact probability increases, in both raw and KR corrected heatmaps, between heterochromatic and euchromatic regions and across chromosome arms (Figures 6D, S19). In particular, the whole genome comparison suggests the individual chromosomes are more apt to interact, which depletes the weak chromosome territories typically observed in WT datasets and is consistent with the local reduction in intra-chromosomal contacts (Figure 6D). Quantifying gains in inter-chromosomal contacts confirms these observations, as contacts between heterochromatic and euchromatic bins, as well as interactions between two euchromatic bins, are increased (Figure 6E). Together, we conclude that the heterochromatin bundle of a Δ*cdp-2*;Δ*dim-2* strain is less compact and more promiscuous following the gains in histone acetylation and the loss of 5^{m}C.

To show how the genome organization changes between the Δ*cdp-2* single mutant and the Δ*cdp-2*;Δ*dim-2* double mutant, we compared the *Dpn*II Hi-C data of these two genetic backgrounds. Across LG II, the Δ*cdp-2*;Δ*dim-2* strain presents an altered genome topology relative to the Δ*cdp-2* strain, with perhaps stronger gains in contact frequency between heterochromatic and euchromatic regions, yet the regional reduction in euchromatic contacts observed in WT vs. Δ*cdp-2*;Δ*dim-2* heatmaps (e.g., between centromeric flanks) no longer occurs, suggesting this change from WT can be attributed to the gain in heterochromatic acetylation (Figure 6F). Similar changes in contact frequency when comparing Δ*cdp-2* and double mutant data are seen across the other LGs and over entire Neurospora genome (Figures S20, S21). Closer examination of the regional changes in contacts between AT-rich loci and euchromatin highlight how hyperacetylation and 5^{m}C loss in the Δ*cdp-2*;Δ*dim-2* strain impacts genome organization: relative to WT, individual H3K9me3-enriched loci more strongly contact euchromatin, thereby depleting euchromatic clustering, (Figure 6G). These changes are more evident when comparing the Δ*cdp-2*;Δ*dim-2* contact frequencies to those in Δ*cdp-2*: the

509 double mutant gains even more heterochromatic-euchromatic contacts; distant euchromatin is also more
510 frequently interacting in a Δ*cdp-2*;Δ*dim-2* strain, highlighting the genome disorder in a double mutant (Figure
511 6G). We conclude that the hyperacetylation of heterochromatic regions coupled with the loss of $5^{m}C$ in a
512 Δ*cdp-2*;Δ*dim-2* strain compromises the normal chromosome conformation in Neurospora nuclei.
513
514 **Discussion**
515 In this work, we have examined the role of CDP-2 and CHAP, members of constitutive heterochromatin-
516 specific histone deacetylase complex HCHC, in the enrichment of histone PTMs and the organization of the
517 genome in the filamentous fungal model organism *Neurospora crassa*. We found that the increases in
518 heterochromatic acetylation in the Δ*cdp-2* strain caused gains in more distant intra- and inter-chromosomal
519 contacts, while the loss of CHAP manifests as reduced heterochromatic region contacts without strong
520 changes in histone acetylation, although neither gene loss destroyed the Rabl chromosome conformation
521 that is typical of fungal genomes (19), suggesting genome organization can still form to some degree despite
522 HCHC loss. Overall, these data suggest that CDP-2 and CHAP have unique and distinct functions in HCHC that
523 differentially impact genome organization, although we cannot exclude the possibility that misregulated
524 gene expression in HCHC mutants pleiotropically disrupts genome organization. Our model (Figure 7) is that
525 CDP-2 recruits the HDA-1 deacetylase for proper compaction of individual heterochromatic regions to
526 ensure normal genome organization while CHAP may act prior to deacetylation for this compaction.
527 Specifically, the increased acetylation seen with CDP-2 loss presumably opens chromatin fibers and/or
528 loosens the DNA wrapped about histones in heterochromatic nucleosomes, thereby facilitating distant
529 contacts between silent regions within the silent "B" compartment at the nuclear periphery (38). In contrast,
530 CHAP may function to compact heterochromatic regions into more dense structures, thereby facilitating
531 inter-heterochromatic region contacts, possibly through its AT hook binding motifs known to directly bind
532 AT-rich DNA (59). Since both proteins are required to recruit the HDA-1 catalytic subunit to heterochromatic
533 regions (59), CDP-2 and CHAP must act prior to HDA-1, and the genome organizational changes we observe
534 reflect strains lacking HDA-1 targeting or the complete loss of HCHC complex formation/function. We
535 speculate that Hi-C of a Δ*hda-1* strain would mimic that of a Δ*cdp-2* strain, with increases in contacts between

distant heterochromatic regions, given the increase in histone acetylation present in strains devoid of HDA-1 (60). We attempted to inhibit HCHC activity in WT cells with the inhibitor Trichostatin A (TSA) and assess genome organization with Hi-C, but WT+TSA strains grown have a severely compromised growth defect – much more so than single HCHC mutants – that precluded any Hi-C library preparation, suggesting off-target effects by TSA on all Neurospora HDACs might compromise the interpretation of any genome topology changes. Notably, the loss of the fourth HCHC complex member, HP1 (in Δ*hpo* strain Hi-C datasets), has a genome topology distinct from that of Δ*cdp-2* or Δ*chap* strains, with the flanking euchromatin emanating from heterochromatic regions having reduced contact probabilities in WT vs. Δ*hpo* datasets, similar to what is observed in a Δ*dim-5* strain lacking H3K9me3 (41). Therefore, HP1 binding to H3K9me3 must occur prior to, or in parallel with, CHAP condensing AT-rich regions; CHAP and HP1 could both act prior to any CDP-2 binding to the chromoshadow domain of HP1 (59) and subsequent HDA-1 recruitment. This proposed mechanism for HCHC activity in Neurospora is unique and contrasts the action of diverse HDAC complexes in yeasts. In *Saccharomyces cerevisiae*, Sirtuin-2 (Sir2; a Class III HDAC)-specific deacetylation is required for the binding of the Sir3/Sir4 dimer onto deacetylated histone tails to form silenced superstructures at heterochromatic loci (e.g., the MAT locus and the telomeres) in the *S. cerevisiae* genome (73, 81, 102, 103). Budding yeast also employs the HDACs Rpd3 (Class I) and HDA-1 (Class II) for euchromatic deacetylation (81, 104–108); Rpd3 forms two distinct HDAC complexes, the Rpd3L (large) and Rpd3S (small) complexes that differ in subunit composition and targets. The Rpd3L deacetylates promoter regions while Rpd3S deacetylates gene bodies; both complexes employ the conserved subunit Sin3p for HDAC complex organization and function (108–110). In *Schizosaccharomyces pombe*, SHREC (***S***nf2/***H***dac-containing ***Re***pressor ***C***omplex) is a multisubunit HDAC targeted to heterochromatic loci by the HP1-homolog Swi6 for transcriptional gene silencing, although SHREC can localize to euchromatin independent of Swi6 (111–113). The Clr3 catalytic subunit in SHREC is homologous to HDA-1 in Neurospora, although three other HDA paralogs and a Rpd3 homolog, among others, exist in Neurospora as well (62). Examination of the other HDACs in Neurospora, or in other fungi using Hi-C and/or ChIP-seq should elucidate how the coordinated action of multiple HDAC complexes in fungi impact genome function.

As previously shown by ChIP qPCR, multiple lysine residues in histone proteins are hyperacetylated upon

563 loss of the HCHC members HDA-1 and CDP-2; the extent of the histone acetylation changes is dependent on
564 which heterochromatic region was assessed as well as which HCHC member was deleted (60). However, this
565 published ChIP qPCR data also hints at the HCHC complex having preferential deacetylation activity for
566 certain lysine residues over others. Our ChIP-seq data provides a genome-wide view of the different
567 acetylation patterns of H3K9 and H4K16 in Δ*cdp-2* and Δ*chap* strains in heterochromatin, although the
568 possibility remains that additional acetylation changes could be observed with the use of DNA spikes in our
569 ChIP-seq experiments (75, 99–101). Specifically, a Δ*cdp-2* strain is hyperacetylated at H4K16 but minimally
570 changed at H3K9 in heterochromatic regions genome wide, arguing that the Neurospora HCHC complex has
571 specificity for certain histone acetyl marks in heterochromatin. We also show that a Δ*chap* strain has minimal
572 H4K16ac enrichment. It remains possible that HP1, or even possibly CDP-2, both of which can bind to
573 H3K9me3 (60, 114, 115), can compensate for CHAP loss to still allow deacetylation by HDA-1. However, the
574 unchanged levels of H3K9ac in a Δ*cdp-2* strain most likely reflects tri-methylation of that residue by the DCDC
575 in these strains (65), given the mutually exclusive deposition of either acetylation or trimethylation on the
576 lysine residue at position 9 on histone H3 (116–118). Future ChIP-seq experiments on other individual
577 histone lysine residues in Δ*cdp-2,* Δ*chap*, or Δ*hda-1* strains should provide global patterns of acetylation
578 changes to dissect HCHC lysine specificity.

579 Interestingly, while Δ*cdp-2* or Δ*chap* strains strongly gain heterochromatin-specific acetylation, relative
580 to WT, in our H4K16ac ChIP-seq data, these mutant strains display no change in euchromatic acetylation,
581 suggesting the HCHC specifically deacetylates heterochromatic regions. Since there is no similarity between
582 the primary structures of the class II Neurospora HDA-1 and the class III HDACs Hst2p and Sir2 in *S.*
583 *cerevisiae*, the latter two of which are known to deacetylate H4K16 (86, 103), it is possible that different
584 HDACs are capable of deacetylating the same histone lysines, and only the targeting mechanism of individual
585 HDAC complexes determines which genomic loci are deacetylated. Given the targeting of HDA-1 to
586 heterochromatic nucleosomes by CHAP binding AT-rich DNA and HP1/CDP-2 binding H3K9me3 (59, 60),
587 the possibility exists that HCHC is only specific to heterochromatic genomic loci for silencing. This explains
588 the large numbers of HCHC mutants, but not other HDACs, recovered from a selection of mutants displaying
589 compromised heterochromatin and cytosine methylation (119). Our data also suggest that a

heterochromatin-specific, yet unknown, histone acetyltransferase (HAT) acetylates H4K16 in a Δ*cdp-2* strain, given that no gains in euchromatic acetylation are observed in this genetic background. An intriguing possibility is that Neurospora modulates HCHC activity – thereby increasing heterochromatic acetylation by this unknown HAT – to rapidly alter fungal genome organization to modulate chromosome structure at specific developmental or cell cycle stages, including S phase, in which fission yeast displays a more open chromosome conformation (120). Conversely, hypoacetylation of mitotic chromatin is required for chromosome condensation and segregation to daughter cells, yet following cytokinesis, chromatin is rapidly acetylated (86, 87), suggesting that dynamic histone acetylation during the cell cycle could be necessary for proper genome organization. Hyperacetylated chromatin at distant genomic loci can also cluster into a novel subcompartment to increase gene expression in BRD4-NUT expressing oncogenic cells (91), in an analogous manner to the hyperacetylated, yet distant heterochromatic regions more strongly interacting in HCHC mutants that we observe here. Together, changes in acetylation patterns may cause novel patterns in genome organization, which may be a general phenomenon of more open and accessible chromatin.

Interestingly, we also observe changes in the deposition of the heterochromatin-specific histone PTM H3K9me3. Specifically, we observed that ~20% of AT-rich regions in a Δ*cdp-2* strain lose H3K9me3, yet there is little effect on the remaining heterochromatic regions, while H3K9me3 levels are modestly enhanced at most AT-rich regions in a Δ*chap* strain. These data again highlight the unique phenotypes of HCHC members. Currently, it is unclear why some AT-rich regions lose H3K9me3 in a Δ*cdp-2* strain, but our preliminary analysis excludes AT-rich region size and extent of AT-richness. It remains possible that the subnuclear positioning of a region, the loss of pairing between the repeats within these regions (121), or DNA motifs found in the transposon relicts of individual regions (122) impact H3K9me3 deposition upon CDP-2 loss; future experiments may provide insight. In contrast, the gain of H3K9me3 in a Δ*chap* strain may result from increased levels or activity of the DCDC, which may be a stopgap mechanism to promote compaction of AT-rich regions by providing more HP1 binding sites. Increases of DCDC proteins are not unique, as the DIM-7 and DIM-9 subunits of the DCDC are increased in a *dim-3* strain to possibly rescue its reduced H3K9me3 levels (123). Our data suggest that WT heterochromatic nucleosomes are not saturated with H3K9me3, given that greater levels of H3K9me3 are possible in some mutant HCHC strains. Moreover, previous work has

shown that H3K9me3 changes can impact the deposition of the repressive di- or tri-methylation of lysine 27 on histone H3 (H3K27me2/3), which denotes facultative heterochromatin in Neurospora. In DCDC deficient strains, H3K27me2/3 relocates to AT-rich genomic loci (116, 124) suggesting altered H3K9me3 patterns in constitutive heterochromatin result in novel facultative heterochromatin patterns. While ChIP qPCR showed minimal changes of H3K27me2/3 at a few loci in HCHC deletion strains (116), examination of the global enrichment of H3K27me2/3 in HCHC deficient backgrounds would be prudent, given the changes in H3K9me3 deposition we report here.

Changes in H3K9me3 are most apparent in the Δ*cdp-2*;Δ*dim-2* double mutant strain, which like the single Δ*cdp-2* mutant, has H3K9me3 loss at ~20% of AT-rich regions, but the remaining heterochromatic regions gain considerable H3K9me3 enrichment. Here, AT-rich regions to be silenced in the Δ*cdp-2*;Δ*dim-2* double mutant are hyperacetylated at H4K16 to a comparable level to the Δ*cdp-2* single mutant, yet there is no cytosine methylation present. Importantly, the genome organization of this double mutant is quite disordered: the AT-rich regions that normally form heterochromatin no longer segregate from euchromatin despite greater H3K9me3 deposition (and presumably HP1 binding). These results may explain the severe growth defect of the Δ*cdp-2*;Δ*dim-2* strain (60): the improper positioning of AT-rich regions into the center of the nucleus may cause aberrant transcriptional profiles, especially considering that heterochromatic-euchromatic contacts are required for proper gene expression in filamentous fungi (39, 125). Perhaps the increased H3K9me3 enrichment in the Δ*cdp-2*;Δ*dim-2* strain is a "last resort" by the fungus to repress AT-rich region transcription in the center of the nucleus: increased H3K9me3 and HP1 compaction could restrict access to the underlying DNA in any mislocalized chromatin to prevent RNA Pol II recruitment. Total RNA sequencing or RNA Pol II ChIP-seq could elucidate this possibility. An important, unanswered question is how H3K9me3 enrichment is increased. We hypothesize that reduced AT-rich region compaction, observed in both Δ*chap* and Δ*cdp-2*;Δ*dim-2* strains, signals for increased H3K9me3 deposition. Consistent with this hypothesis, disorder of nucleosomes in intergenic regions of the genome causes subtle increases in H3K9me3 in Neurospora *dim-1* strains (126), yet additional work is needed to assess this possibility in HCHC mutants.

Importantly, our double mutant Hi-C results suggests that cytosine methylation may have a protective role in maintaining the compartmentalization of chromatin in genome organization: the presence of $5^{m}C$ on

644 DNA may maintain segregation of heterochromatin from euchromatin when these AT-rich regions are
645 hyperacetylated. Specifically, only in strains devoid of both CDP-2 and DIM-2 are AT-rich heterochromatic
646 regions more apt to contact euchromatin. This change in genome organization is not seen in the single Δ*cdp-*
647 *2* mutant, where despite increases in inter-heterochromatic region contacts, silent and active chromatin
648 remain segregated. We speculate that the additional methyl groups added onto DNA allow heterochromatic
649 regions to remain associated at the nuclear periphery, either through active recruitment by a methylated-
650 DNA binding protein (52, 127, 128) or passively by Liquid-Liquid Phase Separation (129, 130). It seems
651 plausible that this loss of chromatin compartmentalization can only occur in strains with compromised
652 heterochromatin, such as in a Δ*cdp-2* background where AT-rich regions gain histone acetylation; we expect
653 a single Δ*dim-2* strain to have few changes in its chromosome conformation considering that the normal
654 heterochromatic machinery (e.g., the DCDC, the HCHC complex, HP1, etc.) is present and no improper
655 hyperacetylation occurs. Consistent with this hypothesis, the $5^{m}C$ increases in most heterochromatic regions
656 observed in a Δ*cdp-2* strain (59, 60) may be necessary to faithfully maintain this chromatin segregation,
657 although the signal to increase $5^{m}C$ catalysis is currently unknown. One intriguing, yet untested, hypothesis
658 is that cells temporarily increase heterochromatic region acetylation during the S phase of the cell cycle to
659 increase chromatin accessibility for genome replication, as opposed to the hypoacetylation observed in M
660 phase (85–88); hypermethylation of AT-rich DNA would maintain chromatin segregation by maintaining
661 heterochromatic loci at the nuclear periphery to ensure that no aberrant transcription of AT-rich regions
662 occurs. All told, cytosine methylation may safeguard the proper chromosome conformation during
663 interphase in conditions where the H3K9me3/HP1-mediated compaction of constitutive heterochromatin is
664 relaxed or compromised. Future experiments should discern if $5^{m}C$ has a similar role for maintaining genome
665 topology in fungal pathogens or higher eukaryotes.
666
667 **Materials and Methods**
668 *Strains and growth conditions*
669 *Neurospora crassa* strains WT N150 or N3752 (both strains are independent propagate strains of 74-
670 OR23-IVA [FGSC #2489]), N3767 (*mat a; his-3 Δcdp-2::hph*), N3613 (*mat A;* Δ*chap::hph*), and N6144 (mat ?;

671 Δ*cdp-2::hph*; Δ*dim-2::hph*) were a gift from Eric U. Selker (University of Oregon). All strains were grown
672 under standard conditions (e.g., 1x Vogels + sucrose media, with necessary supplements) (131).
673
674 *Hi-C library construction*
675 *In situ* Hi-C (32, 120) libraries, which capture ligation products in the nucleus, were constructed as
676 previously described (39), using either the restriction enzyme *Dpn*II (^GATC) to mainly assess euchromatic
677 contacts or the restriction enzyme *Mse*I (T^TAA) to predominantly capture heterochromatic contacts. The
678 entire *in situ* Hi-C protocol adapted for *Neurospora crassa* by isolating spheroplasts is provided in
679 Supplemental File S1. Briefly, Neurospora cultures were grown for four hours at 32°C, crosslinked with
680 formaldehyde and quenched with tris, and treated with a beta-glucanase (Vinotaste) to form spheroplasts.
681 For Hi-C library construction, crosslinked spheroplasts containing 3.5 µg of DNA were disrupted by bead
682 beating (using 150-212 µm Acid Washed Glass Beads [Sigma Aldrich, # G1145-10G]) and the isolated nuclei
683 were made porous by treatment of SDS at 62°C for seven minutes. Nuclear chromatin was digested with the
684 appropriate restriction enzyme (*Dpn*II or *Mse*I; New England Biolabs [NEB]), and overhangs were filled in
685 with Klenow fragment (NEB) using Biotin-14-dATP (Invitrogen, # 19524-016) as well as the standard dTTP,
686 dGTP, and dCTP nucleotides. Blunt-ended fragments were ligated in the nucleus with T4 DNA ligase (NEB),
687 and the resulting DNA loops were purified, Biotin-dATP was removed from unligated ends with T4 DNA
688 polymerase (NEB), and DNA loops were sheared with a Bioruptor Pico (Diagenode). Ligation products were
689 purified with Streptavidin beads (M280 Dynabeads, Invitrogen, # 112.05D), and libraries for Illumina based
690 high-throughput sequencing were constructed with an NEB NEXT Ultra II kit (NEB) per the manufacturer's
691 protocol, except that only eight PCR cycles were used for library amplification to minimize depletion of AT-
692 rich regions in the Neurospora genome (132). Hi-C libraries were sequenced on an Illumina HiSeq 4000 (as
693 100 nucleotide [nt] paired end reads) or an Illumina NovaSeq 6000 (as 59 nt paired end reads) at the
694 University of Oregon Genomics and Cell Characterization Core Facility.
695
696 *Bioinformatic analyses of Hi-C datasets*
697 All analyses were performed, and all Hi-C images generated, with the HiCExplorer program package (96),

as previously reported (39). Previously published *Dpn*II and *Mse*I *in situ* Hi-C data from the WT strain N150 was obtained from the National Center for Biotechnology Information (NCBI) Gene Expression Omnibus (GEO) accession number GSE173593 (39). To normalize WT datasets to compare to mutant strain datasets, the number of total reads were extracted (using the sed command) from the WT R1 and R2 fastq files to provide the number of WT valid reads equal to mutant dataset valid read numbers. Reads were mapped to the previously established nc14 *Neurospora crassa* genome (39) with bowtie2 (133), and used to build the contact matrix with hicBuildMatrix (96); resulting contact matrices were used for all downstream applications, as previously performed (39). Contact quantification was performed by converting hdf5 matrix files to a homer format and counts were extracted into NxN array with the python script dataconvert.py; the python script epigenetic-mark-Quant_v2.py counts intra- and inter-chromosomal bins enriched for specific histone PTMs. Python scripts are available at https://github.com/Klocko-lab/Chip_Quantification).

Chromatin Immunoprecipitation-sequencing (ChIP-seq) library construction

ChIP-seq was performed essentially as previously described (53, 126), except that lysing of cells and shearing of chromatin occurred simultaneously with a Bioruptor Pico (Diagenode), using a 15 minute cycle of 30 seconds of sonication and 30 seconds off, in the presence of Halt Protease and Phosphatase Inhibitor Cocktail (Thermo Fisher Scientific, # 78441); protein A/G magnetic agarose beads (Pierce/Thermo Scientific, # PI78609) purified the antibody/chromatin complex; final ChIP-DNA quantification was performed using the Qubit 3.0 HS method; library barcoding was performed using the NEBNext Ultra II barcoding kit for Illumina sequencing (NEB) per the manufacturer's protocols except that eight PCR cycles were used for the final library generation to minimize AT-rich DNA depletion (132). ChIP-seq libraries were sequenced on an Illumina NovaSeq 6000 (Genomics and Cell Characterization Core Facility, University of Oregon). The Klocko Lab ChIP-seq protocol is provided in Supplemental File S2.

Bioinformatic analyses of ChIP-seq datasets

Raw ChIP-seq data files, as fastq files, were mapped to version 14 of the *Neurospora crassa* genome (nc14) (39) with bowtie2 (133), and output sam files were converted to sorted bam files using samtools

(134), which were used by Deeptools (135) to produce bedgraph and bigwig files, normalized by Reads per Kilobase Per Million Reads (RPKM), for display on the Integrative Genomics Viewer (IGV) (98); IGV images were used for figure creation. Deeptools was also used to create average enrichment signal profiles and heatmaps using bed files for heterochromatic regions (126) or genes. For box plots of the average signal of all features, the average enrichment value per bin for each flanking region was calculated and averaged to obtain a normalization factor to correct the average signal internal to the region; these corrected average signals were plotted in box plots using R and R studio (136, 137). WT H3K9me3 (merged from NCBI GEO accession numbers GSE68897 and GSE98911), WT CenH3 (NCBI GEO accession number GSE71024) and SET-2 H3K27ac (NCBI GEO accession number GSE118495) datasets were previously published (41, 54, 116, 126).

Data availability

All *Neurospora crassa* strains are available upon request. The *in situ* Hi-C and ChIP-seq high-throughput sequencing data generated for this manuscript have been deposited to the NCBI GEO public repository under the superseries accession number GSE232935; the series accession number GSE232933 reports the ChIP-seq data, while the series accession number GSE232934 reports the Hi-C data.

Acknowledgements

The authors wish to thank UCCS students Andrew Reckard, Sara Rodriguez, Yulia Shtanko, Victoria Toscano, and Farh Kaddar for assistance with library generation, initial data analysis, or critical reading of the manuscript text, Doug Turnbull and Jeff Bishop (University of Oregon Genomics and Cell Characterization Core Facility) for Illumina library sequencing service, and all Klocko lab members as well as UCCS Department of Chemistry & Biochemistry colleagues for helpful comments and discussions. Funding was provided by start-up funds from the UCCS College of Letters, Arts, and Sciences and an Academic Research Enhancement Award (AREA) grant from the National Institutes of Health (1R15GM140396-01) to A.D.K.

References

1. B. Bonev, G. Cavalli, Organization and function of the 3D genome. *Nat Rev Genet* 17, 661–678 (2016).

752 2. T. Cremer, C. Cremer, Chromosome territories, nuclear architecture and gene regulation in mammalian
753 cells. *Nat Rev Genet* 2, 292–301 (2001).

754 3. T. Misteli, Beyond the Sequence: Cellular Organization of Genome Function. *Cell* 128, 787–800 (2007).

755 4. J. Dekker, Gene Regulation in the Third Dimension. *Science* 319, 1793–1794 (2008).

756 5. T. Sexton, G. Cavalli, The Role of Chromosome Domains in Shaping the Functional Genome. *Cell* 160,
757 1049–1059 (2015).

758 6. C.-T. Ong, V. G. Corces, Enhancer function: new insights into the regulation of tissue-specific gene
759 expression. *Nat Rev Genet* 12, 283–293 (2011).

760 7. M. Yu, B. Ren, The Three-Dimensional Organization of Mammalian Genomes. *Annu Rev Cell Dev Bi* 33, 1–
761 25 (2017).

762 8. E. E. M. Furlong, M. Levine, Developmental enhancers and chromosome topology. *Science* 361, 1341–
763 1345 (2018).

764 9. M. Falk, *et al.*, Heterochromatin drives compartmentalization of inverted and conventional nuclei. *Nature*
765 570, 395–399 (2019).

766 10. A. J. Shatkin, E. L. Tatum, Electron Microscopy of Neurospora crassa Mycelia. *J Biophysical Biochem Cytol*
767 6, 423–426 (1959).

768 11. W. W. Franke, Nuclear envelopes. Structure and biochemistry of the nuclear envelope. *Philosophical*
769 *Transactions Royal Soc Lond Ser B Biological Sci* 268, 67–93 (1974).

770 12. A. Buchwalter, J. M. Kaneshiro, M. W. Hetzer, Coaching from the sidelines: the nuclear periphery in
771 genome regulation. *Nat Rev Genet* 20, 39–50 (2019).

772 13. S. Schoenfelder, *et al.*, Preferential associations between co-regulated genes reveal a transcriptional
773 interactome in erythroid cells. *Nat Genet* 42, 53–61 (2010).

774 14. B. Tolhuis, R.-J. Palstra, E. Splinter, F. Grosveld, W. de Laat, Looping and Interaction between
775 Hypersensitive Sites in the Active β-globin Locus. *Mol Cell* 10, 1453–1465 (2002).

776 15. J. R. Dixon, *et al.*, Integrative detection and analysis of structural variation in cancer genomes. *Nat Genet*
777 50, 1388–1398 (2018).

778 16. Z. Xu, *et al.*, Structural variants drive context-dependent oncogene activation in cancer. *Nature*, 1–9
779 (2022).

780 17. P. A. Northcott, *et al.*, Enhancer hijacking activates GFI1 family oncogenes in medulloblastoma. *Nature*
781 511, 428–34 (2014).

782 18. W. A. Flavahan, *et al.*, Insulator dysfunction and oncogene activation in IDH mutant gliomas. *Nature* 529,
783 110–114 (2016).

784 19. D. E. Torres, A. T. Reckard, A. D. Klocko, M. Seidl, Nuclear Genome Organization in Fungi: From Gene
785 folding to Rabl Chromosomes. *FEMS Microbiology Reviews* (2023).

20. K. Luger, A. W. Mäder, R. K. Richmond, D. F. Sargent, T. J. Richmond, Crystal structure of the nucleosome core particle at 2.8 Å resolution. *Nature* 389, 251–260 (1997).

21. K. Luger, T. J. Richmond, DNA binding within the nucleosome core. *Curr Opin Struc Biol* 8, 33–40 (1998).

22. E. I. Campos, D. Reinberg, Histones: Annotating Chromatin. *Annu Rev Genet* 43, 559–599 (2009).

23. S. S. P. Rao, *et al.*, Cohesin Loss Eliminates All Loop Domains. *Cell* 171, 305-320.e24 (2017).

24. T. Mizuguchi, *et al.*, Cohesin-dependent globules and heterochromatin shape 3D genome architecture in S. pombe. *Nature* 516, 432–435 (2014).

25. J. H. Haarhuis, B. D. Rowland, Cohesin: building loops, but not compartments. *Embo J* 36, 3549–3551 (2017).

26. I. F. Davidson, J.-M. Peters, Genome folding through loop extrusion by SMC complexes. *Nat Rev Mol Cell Bio* 22, 445–464 (2021).

27. B. W. Bauer, *et al.*, Cohesin mediates DNA loop extrusion by a "swing and clamp" mechanism. *Cell* 184, 5448-5464.e22 (2021).

28. Y. Kim, Z. Shi, H. Zhang, I. J. Finkelstein, H. Yu, Human cohesin compacts DNA by loop extrusion. *Science* 366, 1345–1349 (2019).

29. E. de Wit, *et al.*, CTCF Binding Polarity Determines Chromatin Looping. *Mol Cell* 60, 676–684 (2015).

30. A. L. Sanborn, *et al.*, Chromatin extrusion explains key features of loop and domain formation in wild-type and engineered genomes. *Proc National Acad Sci* 112, E6456–E6465 (2015).

31. J. R. Dixon, *et al.*, Topological Domains in Mammalian Genomes Identified by Analysis of Chromatin Interactions. *Nature* 485, 376–380 (2012).

32. S. S. P. Rao, *et al.*, A 3D Map of the Human Genome at Kilobase Resolution Reveals Principles of Chromatin Looping. *Cell* 159, 1665–1680 (2014).

33. R. D. Acemel, *et al.*, A single three-dimensional chromatin compartment in amphioxus indicates a stepwise evolution of vertebrate Hox bimodal regulation. *Nat Genet* 48, 336–341 (2016).

34. J. Dekker, E. Heard, Structural and functional diversity of Topologically Associating Domains. *Febs Lett* 589, 2877–2884 (2015).

35. A. S. Hansen, C. Cattoglio, X. Darzacq, R. Tjian, Recent evidence that TADs and chromatin loops are dynamic structures. *Nucleus* 9, 20–32 (2018).

36. M. Imakaev, *et al.*, Iterative correction of Hi-C data reveals hallmarks of chromosome organization. *Nat Methods* 9, 999–1003 (2012).

37. T. Cremer, M. Cremer, Chromosome territories. *Csh Perspect Biol* 2, a003889 (2010).

38. E. Lieberman-Aiden, *et al.*, Comprehensive Mapping of Long-Range Interactions Reveals Folding Principles of the Human Genome. *Science* 326, 289–293 (2009).

819 39. S. Rodriguez, *et al.*, The genome organization of Neurospora crassa at high resolution uncovers
820 principles of fungal chromosome topology. *G3 Genes Genomes Genetics* (2022)
821 https:/doi.org/10.1093/g3journal/jkac053.

822 40. M. F. Seidl, *et al.*, Repetitive Elements Contribute to the Diversity and Evolution of Centromeres in the
823 Fungal Genus Verticillium. *Mbio* 11, e01714-20 (2020).

824 41. J. M. Galazka, *et al.*, Neurospora chromosomes are organized by blocks of importin alpha-dependent
825 heterochromatin that are largely independent of H3K9me3. *Genome Res* 26, 1069–1080 (2016).

826 42. D. J. Winter, *et al.*, Repeat elements organise 3D genome structure and mediate transcription in the
827 filamentous fungus Epichloë festucae. *Plos Genet* 14, e1007467 (2018).

828 43. M. R. Speicher, N. P. Carter, The new cytogenetics: blurring the boundaries with molecular biology. *Nat*
829 *Rev Genet* 6, 782–792 (2005).

830 44. C. Hoencamp, *et al.*, 3D genomics across the tree of life reveals condensin II as a determinant of
831 architecture type. *Science* 372, 984–989 (2021).

832 45. L. S. Burrack, *et al.*, Neocentromeres Provide Chromosome Segregation Accuracy and Centromere
833 Clustering to Multiple Loci along a Candida albicans Chromosome. *Plos Genet* 12, e1006317 (2016).

834 46. G. Yao, *et al.*, Gapless genome assembly of Fusarium verticillioides, a filamentous fungus threatening
835 plant and human health. *Sci Data* 10, 229 (2023).

836 47. D. E. Torres, A. T. Reckard, A. D. Klocko, M. F. Seidl, Nuclear genome organization in fungi: From gene
837 folding to Rabl chromosomes. *Fems Microbiol Rev* (2023) https:/doi.org/10.1093/femsre/fuad021.

838 48. A. D. Klocko, *et al.*, Normal chromosome conformation depends on subtelomeric facultative
839 heterochromatin in Neurospora crassa. *Proc National Acad Sci* 113, 15048–15053 (2016).

840 49. J. E. Galagan, *et al.*, The genome sequence of the filamentous fungus Neurospora crassa. *Nature* 422,
841 859–868 (2003).

842 50. K. A. Borkovich, *et al.*, Lessons from the Genome Sequence of Neurospora crassa : Tracing the Path from
843 Genomic Blueprint to Multicellular Organism. *Microbiol Mol Biol R* 68, 1–108 (2004).

844 51. Z. A. Lewis, *et al.*, Relics of repeat-induced point mutation direct heterochromatin formation in
845 Neurospora crassa. *Genome Res* 19, 427–437 (2009).

846 52. M. R. Rountree, E. U. Selker, DNA methylation and the formation of heterochromatin in Neurospora
847 crassa. *Heredity* 105, 38–44 (2010).

848 53. K. Jamieson, M. R. Rountree, Z. A. Lewis, J. E. Stajich, E. U. Selker, Regional control of histone H3 lysine 27
849 methylation in Neurospora. *Proc National Acad Sci* 110, 6027–6032 (2013).

850 54. V. T. Bicocca, T. Ormsby, K. K. Adhvaryu, S. Honda, E. U. Selker, ASH1-catalyzed H3K36 methylation
851 drives gene repression and marks H3K27me2/3-competent chromatin. *Elife* 7, e41497 (2018).

852 55. H. Tamaru, *et al.*, Trimethylated lysine 9 of histone H3 is a mark for DNA methylation in Neurospora
853 crassa. *Nat Genet* 34, 75–79 (2003).

854 56. E. U. Selker, J. N. Stevens, DNA methylation at asymmetric sites is associated with numerous transition
855 mutations. *Proc National Acad Sci* 82, 8114–8118 (1985).

856 57. E. T. Wiles, E. U. Selker, H3K27 methylation: a promiscuous repressive chromatin mark. *Curr Opin Genet*
857 *Dev* 43, 31–37 (2017).

858 58. E. U. Selker, *et al.*, The methylated component of the Neurospora crassa genome. *Nature* 422, 893–897
859 (2003).

860 59. S. Honda, *et al.*, Dual chromatin recognition by the histone deacetylase complex HCHC is required for
861 proper DNA methylation in Neurospora crassa. *Proc National Acad Sci* 113, E6135–E6144 (2016).

862 60. S. Honda, *et al.*, Heterochromatin protein 1 forms distinct complexes to direct histone deacetylation and
863 DNA methylation. *Nat Struct Mol Biol* 19, 471–477 (2012).

864 61. Q. Zhu, M. Ramakrishnan, J. Park, W. J. Belden, Histone H3 lysine 4 methyltransferase is required for
865 facultative heterochromatin at specific loci. *Bmc Genomics* 20, 350 (2019).

866 62. K. M. Smith, *et al.*, H2B- and H3-Specific Histone Deacetylases Are Required for DNA Methylation in
867 Neurospora crassa. *Genetics* 186, 1207–1216 (2010).

868 63. H. Foss, C. Roberts, K. Claeys, E. Selker, Abnormal chromosome behavior in Neurospora mutants
869 defective in DNA methylation. *Science* 262, 1737–1741 (1993).

870 64. Z. A. Lewis, K. K. Adhvaryu, S. Honda, A. L. Shiver, E. U. Selker, Identification of DIM-7, a protein required
871 to target the DIM-5 H3 methyltransferase to chromatin. *Proc National Acad Sci* 107, 8310–8315 (2010).

872 65. Z. A. Lewis, *et al.*, DNA Methylation and Normal Chromosome Behavior in Neurospora Depend on Five
873 Components of a Histone Methyltransferase Complex, DCDC. *Plos Genet* 6, e1001196 (2010).

874 66. J. Dekker, K. Rippe, M. Dekker, N. Kleckner, Capturing Chromosome Conformation. *Science* 295, 1306–
875 1311 (2002).

876 67. S. I. S. Grewal, S. Jia, Heterochromatin revisited. *Nat Rev Genetics* 8, 35–46 (2007).

877 68. A. J. Courtney, A. R. Ferraro, A. D. Klocko, Z. A. Lewis, "Chromatin Structure and Function in Neurospora
878 crassa." in *The Mycota, A Comprehensive Treatise on Fungi as Experimental Systems, Third Edition for Basic*
879 *and Applied Research, Genetics and Biotechnology*, J. P. Benz, K. Schipper, Eds. (Springer Nature Switzerland
880 AG, 2020), pp. 3–24.

881 69. T. Jenuwein, C. D. Allis, Translating the Histone Code. *Science* 293, 1074–1080 (2001).

882 70. F. Zenk, *et al.*, HP1 drives de novo 3D genome reorganization in early Drosophila embryos. *Nature* 593,
883 289–293 (2021).

884 71. A. Eberharter, P. B. Becker, Histone acetylation: a switch between repressive and permissive chromatin.
885 *Embo Rep* 3, 224–229 (2002).

886 72. Y.-J. C. Chen, E. Koutelou, S. Y. R. Dent, Now open: Evolving insights to the roles of lysine acetylation in
887 chromatin organization and function. *Mol Cell* 82, 716–727 (2022).

888 73. D. M. Thurtle, J. Rine, The molecular topography of silenced chromatin in Saccharomyces cerevisiae.
889 *Gene Dev* 28, 245–258 (2014).

890 74. B. J. E. Martin, *et al.*, Transcription shapes genome-wide histone acetylation patterns. *Nat Commun* 12,
891 210 (2021).

892 75. J. N. McKnight, J. W. Boerma, L. L. Breeden, T. Tsukiyama, Global Promoter Targeting of a Conserved
893 Lysine Deacetylase for Transcriptional Shutoff during Quiescence Entry. *Mol Cell* 59, 732–743 (2015).

894 76. A. R. Ferraro, *et al.*, Chromatin accessibility profiling in Neurospora crassa reveals molecular features
895 associated with accessible and inaccessible chromatin. *Bmc Genomics* 22, 459 (2021).

896 77. T. Conrad, F. M. G. Cavalli, J. M. Vaquerizas, N. M. Luscombe, A. Akhtar, Drosophila Dosage Compensation
897 Involves Enhanced Pol II Recruitment to Male X-Linked Promoters. *Science* 337, 742–746 (2012).

898 78. S. Fox, *et al.*, Hyperacetylated chromatin domains mark cell type-specific genes and suggest distinct
899 modes of enhancer function. *Nat Commun* 11, 4544 (2020).

900 79. I. Dunham, *et al.*, An integrated encyclopedia of DNA elements in the human genome. *Nature* 489, 57–74
901 (2012).

902 80. D. U. Gorkin, *et al.*, An atlas of dynamic chromatin landscapes in mouse fetal development. *Nature* 583,
903 744–751 (2020).

904 81. E. Seto, M. Yoshida, Erasers of Histone Acetylation: The Histone Deacetylase Enzymes. *Csh Perspect Biol*
905 6, a018713 (2014).

906 82. A. J. Rubin, *et al.*, Lineage-specific dynamic and pre-established enhancer–promoter contacts cooperate
907 in terminal differentiation. *Nat Genet* 49, 1522–1528 (2017).

908 83. R. Siersbæk, *et al.*, Dynamic Rewiring of Promoter-Anchored Chromatin Loops during Adipocyte
909 Differentiation. *Mol Cell* 66, 420-435.e5 (2017).

910 84. M. W. G. Schneider, *et al.*, A mitotic chromatin phase transition prevents perforation by microtubules.
911 *Nature* 609, 183–190 (2022).

912 85. A. Zhiteneva, *et al.*, Mitotic post-translational modifications of histones promote chromatin compaction
913 in vitro. *Open Biol* 7, 170076 (2017).

914 86. B. J. Wilkins, *et al.*, A Cascade of Histone Modifications Induces Chromatin Condensation in Mitosis.
915 *Science* 343, 77–80 (2014).

916 87. M. J. Kruhlak, *et al.*, Regulation of Global Acetylation in Mitosis through Loss of Histone
917 Acetyltransferases and Deacetylases from Chromatin*. *J Biol Chem* 276, 38307–38319 (2001).

918 88. D. Cimini, M. Mattiuzzo, L. Torosantucci, F. Degrassi, Histone Hyperacetylation in Mitosis Prevents Sister
919 Chromatid Separation and Produces Chromosome Segregation Defects. *Mol Biol Cell* 14, 3821–3833 (2003).

920 89. B. Pelham-Webb, *et al.*, H3K27ac bookmarking promotes rapid post-mitotic activation of the
921 pluripotent stem cell program without impacting 3D chromatin reorganization. *Mol Cell* 81, 1732-1748.e8
922 (2021).

90. H. Kang, *et al.*, Dynamic regulation of histone modifications and long-range chromosomal interactions during postmitotic transcriptional reactivation. *Gene Dev* 34, 913–930 (2020).

91. C. D. Rosencrance, *et al.*, Chromatin Hyperacetylation Impacts Chromosome Folding by Forming a Nuclear Subcompartment. *Mol Cell* 78, 112-126.e12 (2020).

92. B. A. Gibson, *et al.*, Organization of Chromatin by Intrinsic and Regulated Phase Separation. *Cell* 179, 470-484.e21 (2019).

93. D. C. Anderson, G. R. Green, K. Smith, E. U. Selker, Extensive and Varied Modifications in Histone H2B of Wild-Type and Histone Deacetylase 1 Mutant Neurospora crassa. *Biochemistry-us* 49, 5244–5257 (2010).

94. J. D. Gessaman, E. U. Selker, Induction of H3K9me3 and DNA methylation by tethered heterochromatin factors in Neurospora crassa. *P Natl Acad Sci Usa* 114, E9598–E9607 (2017).

95. P. A. Knight, D. Ruiz, A fast algorithm for matrix balancing. *Ima J Numer Anal* 33, 1029–1047 (2013).

96. F. Ramírez, *et al.*, High-resolution TADs reveal DNA sequences underlying genome organization in flies. *Nat Commun* 9, 189 (2018).

97. T. Cremer, *et al.*, Rabl's model of the interphase chromosome arrangement tested in Chinise hamster cells by premature chromosome condensation and laser-UV-microbeam experiments. *Hum Genet* 60, 46–56 (1982).

98. J. T. Robinson, *et al.*, Integrative genomics viewer. *Nat Biotechnol* 29, 24–6 (2011).

99. N. Bonhoure, *et al.*, Quantifying ChIP-seq data: a spiking method providing an internal reference for sample-to-sample normalization. *Genome Res* 24, 1157–68 (2014).

100. B. Hu, *et al.*, Biological chromodynamics: a general method for measuring protein occupancy across the genome by calibrating ChIP-seq. *Nucleic Acids Res* 43, gkv670 (2015).

101. D. A. Orlando, *et al.*, Quantitative ChIP-Seq Normalization Reveals Global Modulation of the Epigenome. *Cell Reports* 9, 1163–1170 (2014).

102. D. Moazed, A. Kistler, A. Axelrod, J. Rine, A. D. Johnson, Silent information regulator protein complexes in Saccharomyces cerevisiae: A SIR2/SIR4 complex and evidence for a regulatory domain in SIR4 that inhibits its interaction with SIR3. *Proc National Acad Sci* 94, 2186–2191 (1997).

103. S. Imai, C. M. Armstrong, M. Kaeberlein, L. Guarente, Transcriptional silencing and longevity protein Sir2 is an NAD-dependent histone deacetylase. *Nature* 403, 795–800 (2000).

104. J. Wu, A. A. Carmen, R. Kobayashi, N. Suka, M. Grunstein, HDA2 and HDA3 are related proteins that interact with and are essential for the activity of the yeast histone deacetylase HDA1. *Proc National Acad Sci* 98, 4391–4396 (2001).

105. J. Wu, N. Suka, M. Carlson, M. Grunstein, TUP1 Utilizes Histone H3/H2B–Specific HDA1 Deacetylase to Repress Gene Activity in Yeast. *Mol Cell* 7, 117–126 (2001).

106. S. E. Rundlett, *et al.*, HDA1 and RPD3 are members of distinct yeast histone deacetylase complexes that regulate silencing and transcription. *Proc National Acad Sci* 93, 14503–14508 (1996).

958 107. S. R. V. Knott, C. J. Viggiani, S. Tavaré, O. M. Aparicio, Genome-wide replication profiles indicate an
959 expansive role for Rpd3L in regulating replication initiation timing or efficiency, and reveal genomic loci of
960 Rpd3 function in Saccharomyces cerevisiae. *Gene Dev* 23, 1077–1090 (2009).

961 108. M. J. Carrozza, *et al.*, Histone H3 Methylation by Set2 Directs Deacetylation of Coding Regions by Rpd3S
962 to Suppress Spurious Intragenic Transcription. *Cell* 123, 581–592 (2005).

963 109. Z. Guo, *et al.*, Structure of a SIN3–HDAC complex from budding yeast. *Nat Struct Mol Biol*, 1–8 (2023).

964 110. D. Kadosh, K. Struhl, Repression by Ume6 Involves Recruitment of a Complex Containing Sin3
965 Corepressor and Rpd3 Histone Deacetylase to Target Promoters. *Cell* 89, 365–371 (1997).

966 111. T. Sugiyama, *et al.*, SHREC, an Effector Complex for Heterochromatic Transcriptional Silencing. *Cell*
967 128, 491–504 (2007).

968 112. G. Job, *et al.*, SHREC Silences Heterochromatin via Distinct Remodeling and Deacetylation Modules. *Mol*
969 *Cell* 62, 207–221 (2016).

970 113. T. Yamada, W. Fischle, T. Sugiyama, C. D. Allis, S. I. S. Grewal, The Nucleation and Maintenance of
971 Heterochromatin by a Histone Deacetylase in Fission Yeast. *Mol Cell* 20, 173–185 (2005).

972 114. M. Freitag, P. C. Hickey, T. K. Khlafallah, N. D. Read, E. U. Selker, HP1 Is Essential for DNA Methylation
973 in Neurospora. *Mol Cell* 13, 427–434 (2004).

974 115. S. A. Jacobs, S. Khorasanizadeh, Structure of HP1 Chromodomain Bound to a Lysine 9-Methylated
975 Histone H3 Tail. *Science* 295, 2080–2083 (2002).

976 116. K. Jamieson, *et al.*, Loss of HP1 causes depletion of H3K27me3 from facultative heterochromatin and
977 gain of H3K27me2 at constitutive heterochromatin. *Genome Res* 26, 97–107 (2016).

978 117. A. J. Bannister, T. Kouzarides, Regulation of chromatin by histone modifications. *Cell Res* 21, 381–395
979 (2011).

980 118. T. Zhang, S. Cooper, N. Brockdorff, The interplay of histone modifications – writers that read. *Embo Rep*
981 16, 1467–1481 (2015).

982 119. A. D. Klocko, *et al.*, Selection and Characterization of Mutants Defective in DNA Methylation in
983 Neurospora crassa. *Genetics* 216, genetics.303471.2020 (2020).

984 120. H. Tanizawa, K.-D. Kim, O. Iwasaki, K. Noma, Architectural alterations of the fission yeast genome
985 during the cell cycle. *Nat Struct Mol Biol* 24, 965–976 (2017).

986 121. N. Rhoades, *et al.*, Recombination-independent recognition of DNA homology for meiotic silencing in
987 Neurospora crassa. *Proc National Acad Sci* 118, e2108664118 (2021).

988 122. D. Nguyen, *et al.*, Transposon- and Genome Dynamics in the Fungal Genus Neurospora: Insights from
989 Nearly Gapless Genome Assemblies. *Fungal Genetics Reports* 66 (2022).

990 123. A. D. Klocko, *et al.*, Neurospora Importin α Is Required for Normal Heterochromatic Formation and
991 DNA Methylation. *Plos Genet* 11, e1005083 (2015).

992 124. E. Y. Basenko, *et al.*, Genome-wide redistribution of H3K27me3 is linked to genotoxic stress and
993 defective growth. *Proc National Acad Sci* 112, E6339–E6348 (2015).

994 125. H. M. Kramer, D. E. Cook, G. C. M. van den Berg, M. F. Seidl, B. P. H. J. Thomma, Three putative DNA
995 methyltransferases of Verticillium dahliae differentially contribute to DNA methylation that is dispensable
996 for growth, development and virulence. *Epigenet Chromatin* 14, 21 (2021).

997 126. A. D. Klocko, *et al.*, Nucleosome Positioning by an Evolutionarily Conserved Chromatin Remodeler
998 Prevents Aberrant DNA Methylation in Neurospora. *Genetics* 211, 563–578 (2019).

999 127. R. Meehan, J. D. Lewis, A. P. Bird, Characterization of MeCP2, a vertebrate DNA binding protein with
1000 affinity for methylated DNA. *Nucleic Acids Res* 20, 5085–5092 (1992).

1001 128. E. U. Selker, *et al.*, Induction and maintenance of nonsymmetrical DNA methylation in Neurospora.
1002 *Proc National Acad Sci* 99, 16485–16490 (2002).

1003 129. A. G. Larson, *et al.*, Liquid droplet formation by HP1α suggests a role for phase separation in
1004 heterochromatin. *Nature* 547, 236–240 (2017).

1005 130. A. R. Strom, *et al.*, Phase separation drives heterochromatin domain formation. *Nature* 547, 241–245
1006 (2017).

1007 131. R. H. Davis, *Neurospora: contributions of a model organism* (Oxford University Press, 2000).

1008 132. L. Ji, *et al.*, Methylated DNA is over-represented in whole-genome bisulfite sequencing data. *Frontiers*
1009 *Genetics* 5, 341 (2014).

1010 133. B. Langmead, S. L. Salzberg, Fast gapped-read alignment with Bowtie 2. *Nat Methods* 9, 357–359
1011 (2012).

1012 134. H. Li, *et al.*, The Sequence Alignment/Map format and SAMtools. *Bioinformatics* 25, 2078–2079 (2009).

1013 135. F. Ramírez, *et al.*, deepTools2: a next generation web server for deep-sequencing data analysis. *Nucleic*
1014 *Acids Res* 44, W160-5 (2016).

1015 136. Rs. Team, *RStudio: Integrated Development for R* (RStudio, PBC, 2020).

1016 137. R. C. Team, *R: A language and environment for statistical computing* (R Foundation for Statistical
1017 Computing, 2021).

1018

1019 **Figure Legends**

1020 ***Figure 1.* Δcdp-2 *and* Δchap *strains change the genome organization of a single chromosome in***

1021 **Neurospora crassa.** (A-B) Heatmap of contact probabilities of 20 kilobase (kb) bins across Linkage Group

1022 (LG) II of a (A) wild type (WT) *Neurospora crassa* strain (data from (39)) or a (B) Δ*cdp-2* strain. B. Solid

1023 arrowheads show regions of increased heterochromatic-heterochromatic contacts, while open arrowheads

show decreased heterochromatic-euchromatic contacts. Above the diagonal is the heatmap displaying the raw read count per 20 kb bins generated from an *in situ* Hi-C experiment using the heterochromatin-specific enzyme *Mse*I (recognition sequence T^TAA), while below the diagonal is the heatmap displaying the Knight Ruiz corrected (95, 96) read count per 20 kb bins generated from an *in situ* Hi-C experiment using the euchromatin-specific enzyme *Dpn*II (recognition sequence ^GATC); throughout this work (unless otherwise described), heatmaps are shown in a similar orientation with only one half of a square heatmap being included in figures to allow comparisons (each contact probability heatmap shows identical data reflected about the diagonal). The number of bins (vertical markings) and genomic distance, in Megabases (Mb) (horizontal markings) are shown on the plot axes here and in heatmaps throughout this manuscript. The scale bar (here, below the image) is provided in all figures to indicate the number of mapped reads per bin on a $\log_{10}$ scale (log transformed). Integrative Genomics Viewer (IGV) (98) images of WT CenH3 (red) and/or H3K9me3 (green) ChIP-seq tracks presented above and to the left to indicate the centromeric and heterochromatic regions of LG II, respectively; ChIP-seq enrichment scales shown; similar scales are used for all ChIP-seq enrichment track images in this manuscript. WT H3K9me3 ChIP-seq data is presented for mutant Hi-C images for referencing the normal locations of heterochromatic regions. (C) The fold change in contact strength ($\log_2$ scale) in a Δ*cdp-2* strain relative to a normalized WT strain of *Mse*I *in situ* Hi-C (above diagonal) or *Dpn*II *in situ* Hi-C (below diagonal) datasets; image displayed similarly as in panel A; enhanced region in panel D indicated by the purple line. The open arrowhead indicates a large heterochromatic region that gains internal, possibly nucleosomal contacts at the expense of euchromatic – heterochromatic contacts. (D) Heatmap displaying the contact probability changes between distant heterochromatic regions and the centromere at 10 kb resolution. Image displaying enrichment of H3K9me3 denotes constitutive heterochromatic regions, including the centromere, at the far left. (E) Heatmap of contact probabilities of 20 kb bins across LG II of a Δ*chap* strain, displayed as in panel A. Heatmap below shows the contact probabilities of the right arm of LG II of the Δ*chap* dataset at 10 kb resolution; H3K9me3 enrichment shown to the right. (F-G) The fold change in contact strength ($\log_2$ scale) in a Δ*chap* strain relative to a normalized WT strain, displayed as in panel C, of (F) the entire LG II or (G) the right arm of LG II. (H) Quantification of strongly changed, intra-chromosomal contacts in Δ*cdp-2* or Δ*chap* datasets relative to normalized WT strains of bins

enriched with the indicated histone PTMs, with the first bin being enriched with either H3K9me3 (indicated by asterisk) or H3K27ac and the second bin enriched with another histone PTM. (I) The fold change in contact strength in a Δ*chap* strain relative to a Δ*cdp-2* strain, as displayed in panel C. Arrowheads show the decrease in heterochromatic contacts in a Δ*chap* strain relative to a Δ*cdp-2* strain. (J) The fold change in contact strength of *Mse*I datasets of a Δ*cdp-2* strain (above diagonal) or a Δ*chap* strain (below diagonal) relative to a WT strain at 10 kb resolution.

Figure 2.* Δcdp-2 *and* Δchap *strains alter the genome organization across the entire* Neurospora crassa *genome. (A, D) The fold change in contact strength of the entire genome (all seven chromosomes) in a (A) Δ*cdp-2* strain or (D) a Δ*chap* strain relative to a WT strain of *Mse*I *in situ* Hi-C (above diagonal) or *Dpn*II *in situ* Hi-C (below diagonal) in 20 kb resolution datasets; image displayed similarly as in Figure 1C, with chromosome schematics (black squares indicating centromeres and green ovals showing telomeres) above and left. (B, E) Heatmap of contact probabilities of 20 kb bins between LG II and LG III of a (B) Δ*cdp-2* strain or (E) a Δ*chap* strain, displayed similarly to Figure 1A; image of the H3K9me3 enrichment across those two chromosomes in a WT strain displayed above and left. (C, F) The fold change in contact strength of 20 kb bins between LG II and LG III in a Δ*cdp-2* strain, or (F) a Δ*chap* strain, relative to a WT strain of *Mse*I *in situ* Hi-C datasets, displayed as in panel B. (G) Quantification of strongly changed, inter-chromosomal contacts in Δ*cdp-2* or Δ*chap* datasets relative to a WT strain, as in Figure 1H.

Figure 3. Loss of CDP-2 alters the acetylation of H4K16, but not H3K9, in constitutive heterochromatic regions across the* Neurospora crassa *genome. (A) Images of H4K16ac and H3K9ac ChIP-seq enrichment tracks from WT and Δ*cdp-2* strains, displayed on IGV, of the entire LG II (top) and the terminal 700 kb of LG II right arm from the Neurospora genome (bottom). WT H3K9me3 (116, 126) and SET-2 specific H3K27ac (as assayed in a Δ*ash1*^{Y833F} background (54)) are displayed to indicate heterochromatic and euchromatic genome loci, respectively. Arrowheads in the zoomed in image highlight heterochromatic regions that gain enrichment of H4K16ac in a Δ*cdp-2* strain. (B-C) Average enrichment profiles (top) and heatmaps (bottom) of the H4K16ac enrichment in WT and Δ*cdp-2* strains over (B) the H3K9me3-marked constitutive

heterochromatic regions in a WT strain (scaled to 10 kb in length) or (C) genes (scaled to 2.5 kb in length). The small peak in the middle of panel B most likely reflects the repetitive rDNA gene on LG V (39). (D-E) Boxplots of the normalized H4K16ac signal (see Materials and Methods) of each (D) heterochromatic region or (E) gene in WT and Δ*cdp-2* stains. Asterisks show significant ($p < 0.001$) differences in signal.

Figure 4. Changes in H3K9me3 deposition and genome organization of constitutive heterochromatic regions upon CDP-2 loss across the* Neurospora crassa *genome. (A) Images of H3K9me3 and H4K16ac ChIP-seq enrichment tracks of WT and Δ*cdp-2* strains, displayed on IGV, of the entire LG II (top) and a 400 kb section of the LG II left arm from the Neurospora genome (bottom). The region highlighted in the red box on the right (further zoomed in) shows the changes in H3K9me3 and H4K16ac enrichment for one heterochromatic region. (B) Average enrichment profile (top) and heatmap (bottom) of the H3K9me3 enrichment in WT and Δ*cdp-2* strains over the H3K9me3-marked constitutive heterochromatic regions in a WT strain (scaled to 10 kb in length). (C) Boxplots of the normalized H3K9me3 signal of each heterochromatic region in WT or Δ*cdp-2* stains, as in Figure 3D. (D) Heatmaps of the change in contact probabilities between a Δ*cdp-2* strain and a WT strain of two regions containing at least one AT-rich locus that loses H3K9me3 in a Δ*cdp-2* strain. WT and Δ*cdp-2* H3K9me3 ChIP-seq track images below each Hi-C heatmap. Asterisks indicate the regions that lose H3K9me3, while black arrowheads highlight gains in inter-heterochromatic region contacts in a Δ*cdp-2* strain; white arrowhead shows an inter-heterochromatic interaction that does not gain interactions despite these silent regions being similarly spaced. Zoomed image (left) highlights changes in a 250 kb region of LG I where two AT-rich loci lose H3K9me3 enrichment; pink arrowheads show the gain of H4K16ac in a Δ*cdp-2* strain.

***Figure 5. Loss of CDP-2 and DIM-2 have an increase in H4K16ac with a concomitant gain of H3K9me3 enrichment in constitutive heterochromatic regions in* Neurospora crassa.** (A) Images of H3K9me3 and H4K16ac ChIP-seq enrichment tracks of WT, Δ*cdp-2*, and Δ*cdp-2;*Δ*dim-2* strains, displayed on IGV, of the entire LG II (top) and the terminal 700 kb of LG II right arm from the Neurospora genome (bottom). Asterisks indicate AT-rich regions that lose H3K9me3 enrichment in both Δ*cdp-2* and Δ*cdp-2;*Δ*dim-2* strains. (B,D)

Average enrichment profiles (top) and heatmaps (bottom) of the (B) H4K16ac or (D) H3K9me3 enrichment in WT, Δ*cdp-2*, and Δ*cdp-2;*Δ*dim-2* strains over the H3K9me3-marked constitutive heterochromatic regions in a WT strain (scaled to 10 kb in length). Note that the order of regions is maintained in heatmap groups, highlighting how the same AT-rich regions lose H3K9me3 in both Δ*cdp-2* and Δ*cdp-2;*Δ*dim-2* strains. (C,E) Boxplots of the normalized (C) H4K16ac or (E) H3K9me3 signal (see Materials and Methods) of each heterochromatic region in WT, Δ*cdp-2*, and Δ*cdp-2;*Δ*dim-2* stains, as in Figure 3D.

Figure 6. The genome organization of a* Δcdp-2;Δdim-2 *strain is strongly changed relative to WT, with gains in heterochromatic-euchromatic contacts. (A) Heatmap of raw (above diagonal) or KR corrected (below diagonal) contact probabilities of 20 kb bins across Linkage Group (LG) II of a Δ*cdp-2;*Δ*dim-2* strain, displayed similar to Figure 1B. (B) The fold change in contact strength of LG II in a Δ*cdp-2*;Δ*dim-2* strain relative to a WT strain of *Dpn*II *in situ* Hi-C similarly to Figure 1C. Changes in raw (above diagonal) or KR corrected (below diagonal) contact probabilities are displayed. Arrowheads indicate the heterochromatic regions highlighted in Figure 6G. (C, E) Quantification of strongly changed, (C) intra-chromosomal or (E) inter-chromosomal contacts in Δ*cdp-2* (exact data displayed in Figures 1H or 2G) or Δ*cdp-2*;Δ*dim-2* strains relative to a WT strain, as in Figure 1H. (D) The fold change in contact strength of the entire genome in a Δ*cdp-2*;Δ*dim-2* strain relative to a WT strain of *Dpn*II *in situ* Hi-C, similar to Figure 2A. Changes in raw (above diagonal) or KR corrected (below diagonal) contact probabilities are displayed. (F) The fold change in contact strength of LG II in a Δ*cdp-2*;Δ*dim-2* strain relative to a Δ*cdp-2* strain of *Dpn*II *in situ* Hi-C similarly to Figure 6B. (G) The fold change in raw contact strength of two heterochromatic regions (highlighted by arrowheads in Figures 6B,F) in a Δ*cdp-2*;Δ*dim-2* strain relative to a (top) WT or a (bottom) Δ*cdp-2* strain. H3K9me3 ChIP-seq tracks in a Δ*cdp-2* or a Δ*cdp-2*;Δ*dim-2* strain, as well as genes, are shown in the middle.

***Figure 7. Models of how HCHC mutant strains impact heterochromatin formation and genome organization in* Neurospora crassa.** (A-D) In a WT strain, or in the specified HCHC mutant strains, heterochromatin formation at the level of nucleosomes (left) and organization of two example chromosomes (right) are displayed. At left, in a WT strain (A), the HCHC (HDA-1, CDP-2, HP1, CHAP) complex removes the

acetylation marks (green triangles) from histone tails; CDP-2 can bind H3K9me3 (red hexagons) and is necessary to recruit HDA-1 to heterochromatic, AT-rich DNA (orange lines), while CHAP is necessary for interacting with more distant nucleosomes in AT-rich regions. On deacetylated histone tails, the DCDC (DIM-5/7/9, CUL4, DDB1^{dim-8}, Complex) is necessary for the deposition of H3K9me3, which is bound by HP1 to directly recruit the DNA methyltransferase DIM-2 for cytosine methylation ($5^{m}C$; orange hexagons). At right, the action of both complexes establishes a genome organization in which centromeres (red circles) cluster and associate on one inner nuclear membrane face, while the (sub)telomeres (green circles) associate on the opposing nuclear membrane in Rabl chromosome conformation. Interspersed heterochromatic regions (black circles) on both chromosomes associate on the nuclear periphery as well, with the euchromatic arms of each chromosome more likely to associate in the center of the nucleus. (B) Loss of CDP-2 causes gains in $5^{m}C$ and histone acetylation (green triangles) while maintaining H3K9me3 at some heterochromatic regions (other regions completely lose H3K9me3), which causes increases in distant heterochromatic region contacts (including the gains of smaller heterochromatic region contacts with the centromeres), while inter-chromosomal centromeric contacts are decreased. (C) Loss of CHAP prevents compaction of heterochromatic regions and reduces some heterochromatic region interactions, despite increases in $5^{m}C$ and H3K9me3 while maintaining histone deacetylation. (D) Loss of both CDP-2 and DIM-2 causes gains in histone acetylation and H3K9me3, but heterochromatic regions no longer associate with the nuclear periphery and interact more with euchromatin, thereby increasing in genome disorder.

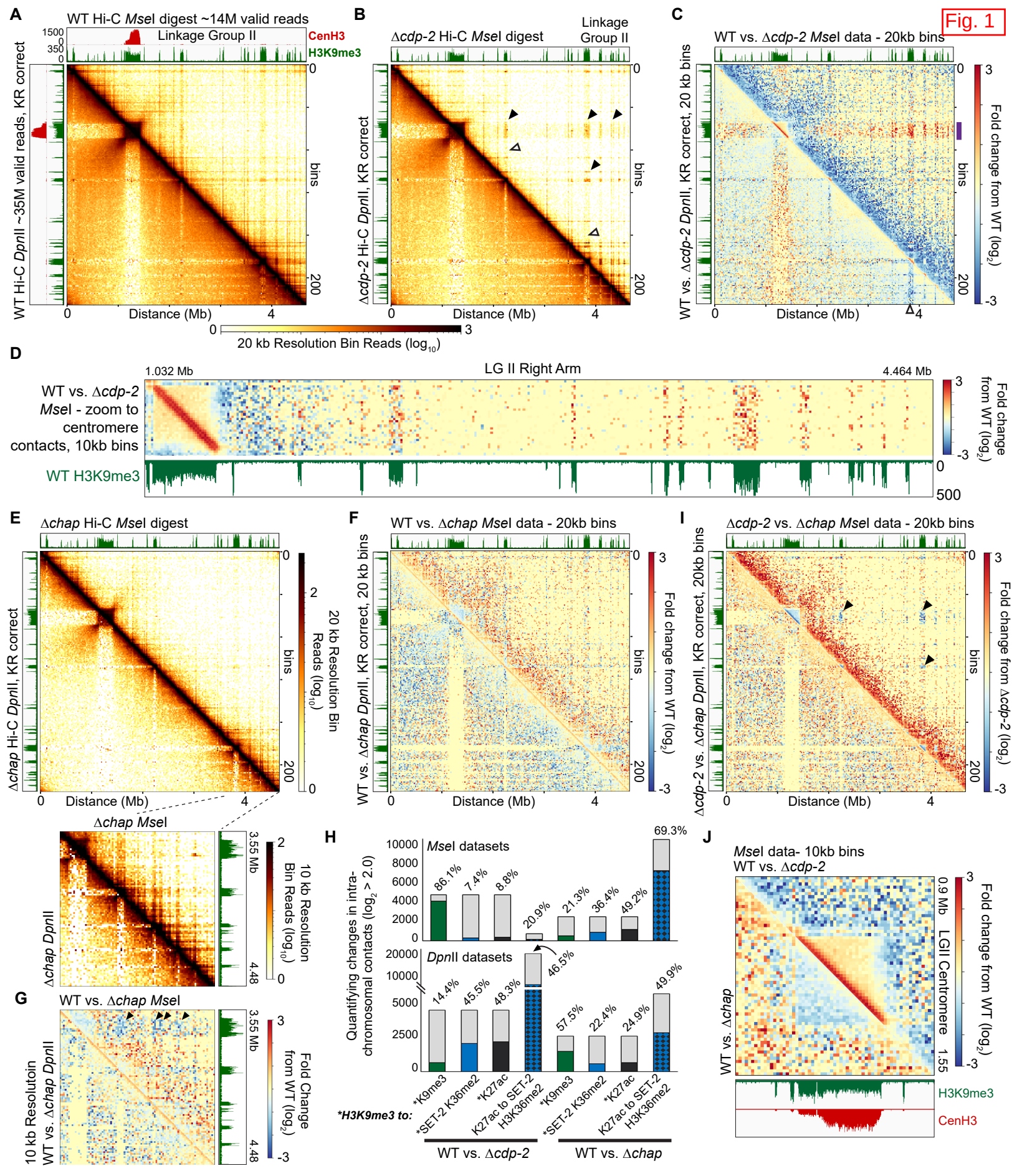
Fig. 1
A
WT Hi-C MseI digest ~14M valid reads
Linkage Group II
CenH3
H3K9me3
WT Hi-C DpnII ~35M valid reads, KR correct
bins
Distance (Mb)
B
Δcdp-2 Hi-C MseI digest
Linkage Group II
Δcdp-2 Hi-C DpnII, KR correct
C
WT vs. Δcdp-2 MseI data - 20kb bins
WT vs. Δcdp-2 DpnII, KR correct, 20 kb bins
Fold change from WT (log2)
20 kb Resolution Bin Reads (log10)
D
1.032 Mb
LG II Right Arm
4.464 Mb
WT vs. Δcdp-2 MseI - zoom to centromere contacts, 10kb bins
WT H3K9me3
E
Δchap Hi-C MseI digest
Δchap Hi-C DpnII, KR correct
20 kb Resolution Bin Reads (log10)
Δchap MseI
Δchap DpnII
10 kb Resolution Bin Reads (log10)
3.55 Mb
4.48
F
WT vs. Δchap MseI data - 20kb bins
WT vs. Δchap DpnII, KR correct, 20 kb bins
I
Δcdp-2 vs. Δchap MseI data - 20kb bins
Δcdp-2 vs. Δchap DpnII, KR correct, 20kb bins
Fold change from Δcdp-2 (log2)
G
WT vs. Δchap MseI
10 kb Resolutoin WT vs. Δchap DpnII
Fold Change from WT (log2)
H
Quantifying changes in intra-chromosomal contacts (log2 > 2.0)
MseI datasets
DpnII datasets
86.1%
7.4%
8.8%
20.9%
21.3%
36.4%
49.2%
69.3%
14.4%
45.5%
48.3%
46.5%
57.5%
22.4%
24.9%
49.9%
*K9me3
*SET-2 K36me2
*K27ac
K27ac to SET-2 H3K36me2
*H3K9me3 to:
WT vs. Δcdp-2
WT vs. Δchap
J
MseI data- 10kb bins
WT vs. Δcdp-2
WT vs. Δchap
0.9 Mb
LGII Centromere
1.55
H3K9me3
CenH3

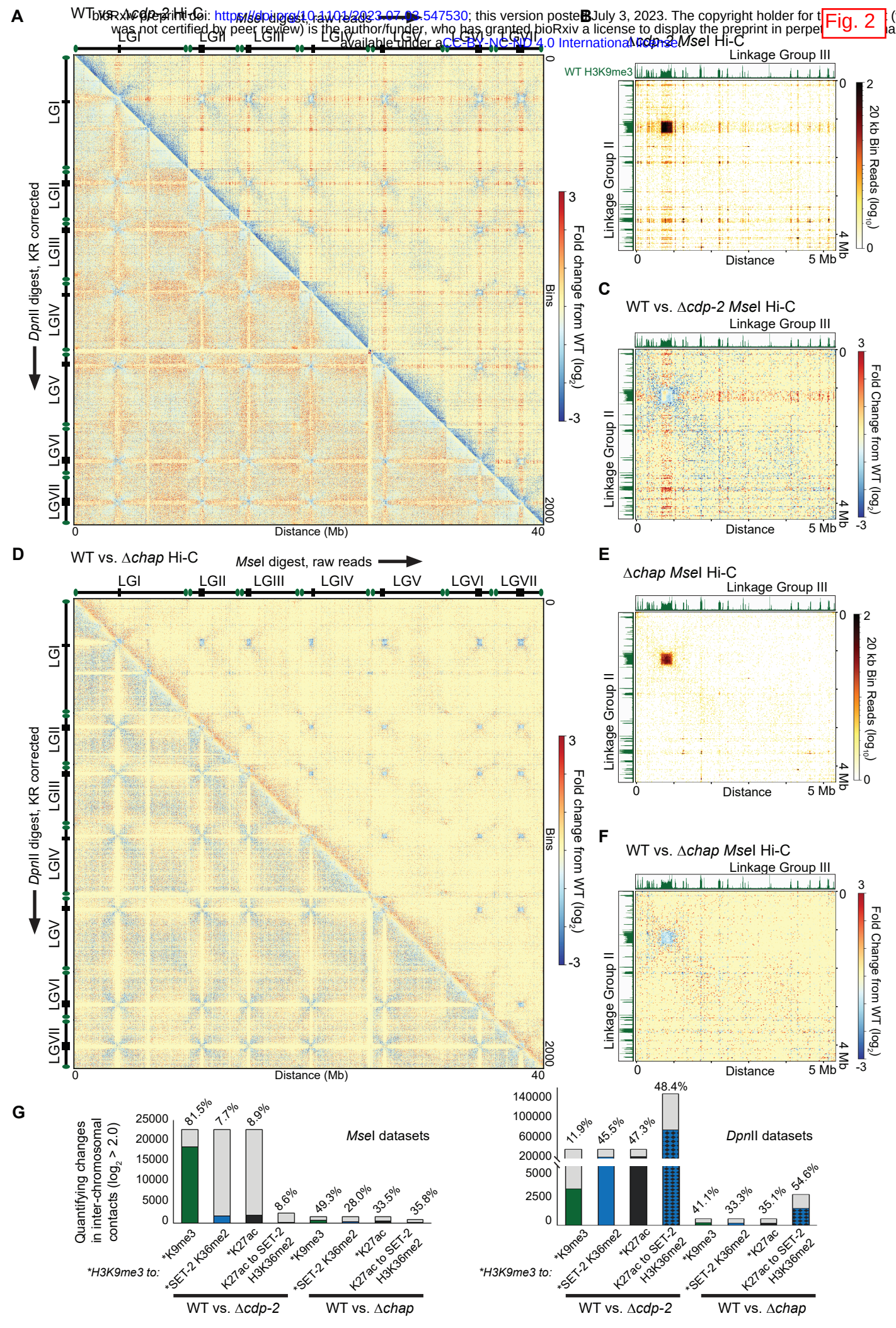

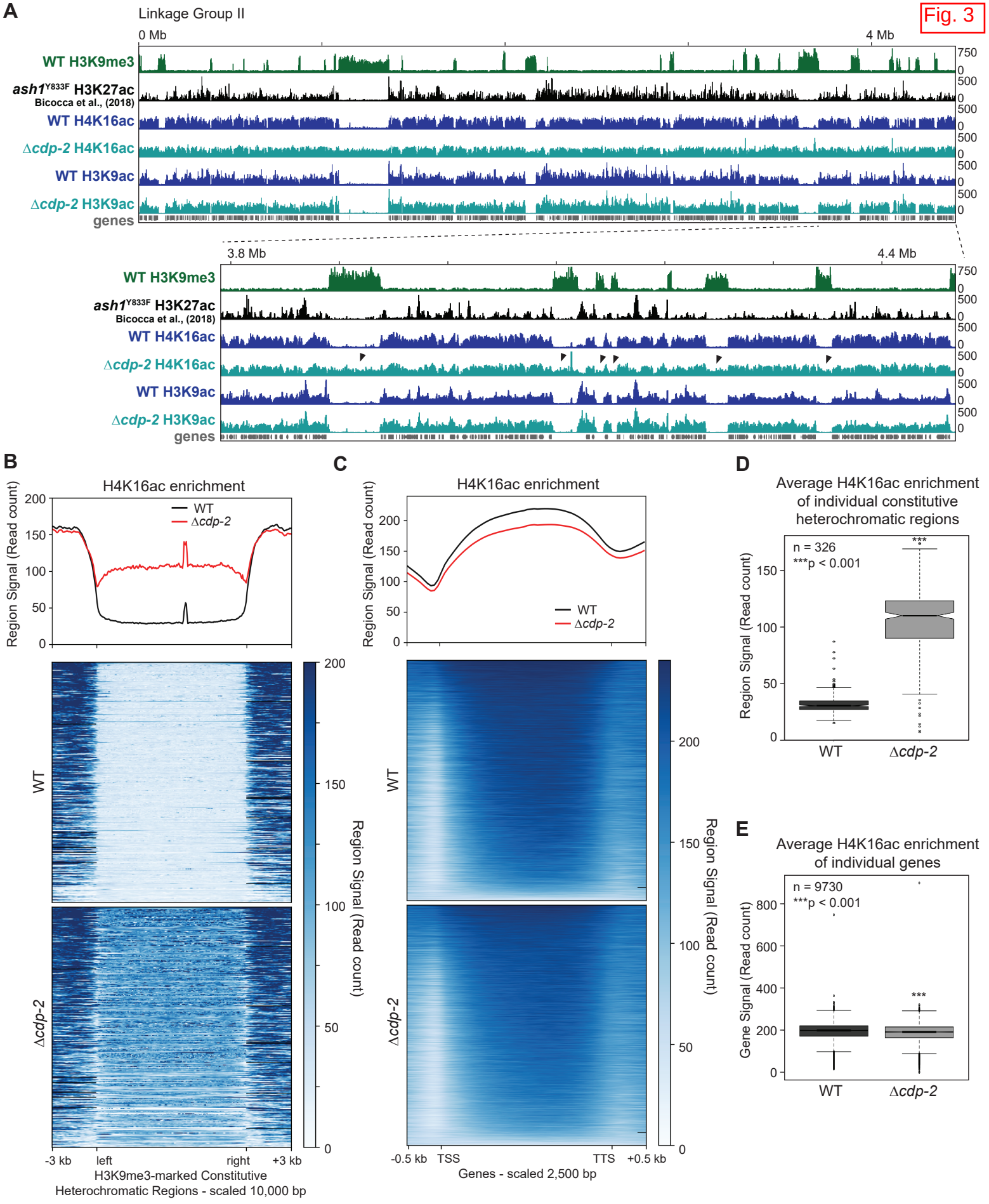
A
Linkage Group II
Fig. 3
0 Mb
4 Mb
WT H3K9me3
ash1Y833F H3K27ac
Bicocca et al., (2018)
WT H4K16ac
Δcdp-2 H4K16ac
WT H3K9ac
Δcdp-2 H3K9ac
genes
3.8 Mb
4.4 Mb
B
H4K16ac enrichment
Region Signal (Read count)
WT
Δcdp-2
-3 kb
left
right
+3 kb
H3K9me3-marked Constitutive
Heterochromatic Regions - scaled 10,000 bp
C
H4K16ac enrichment
-0.5 kb
TSS
TTS
+0.5 kb
Genes - scaled 2,500 bp
D
Average H4K16ac enrichment
of individual constitutive
heterochromatic regions
n = 326
***p < 0.001
E
Average H4K16ac enrichment
of individual genes
n = 9730
***p < 0.001
Gene Signal (Read count)

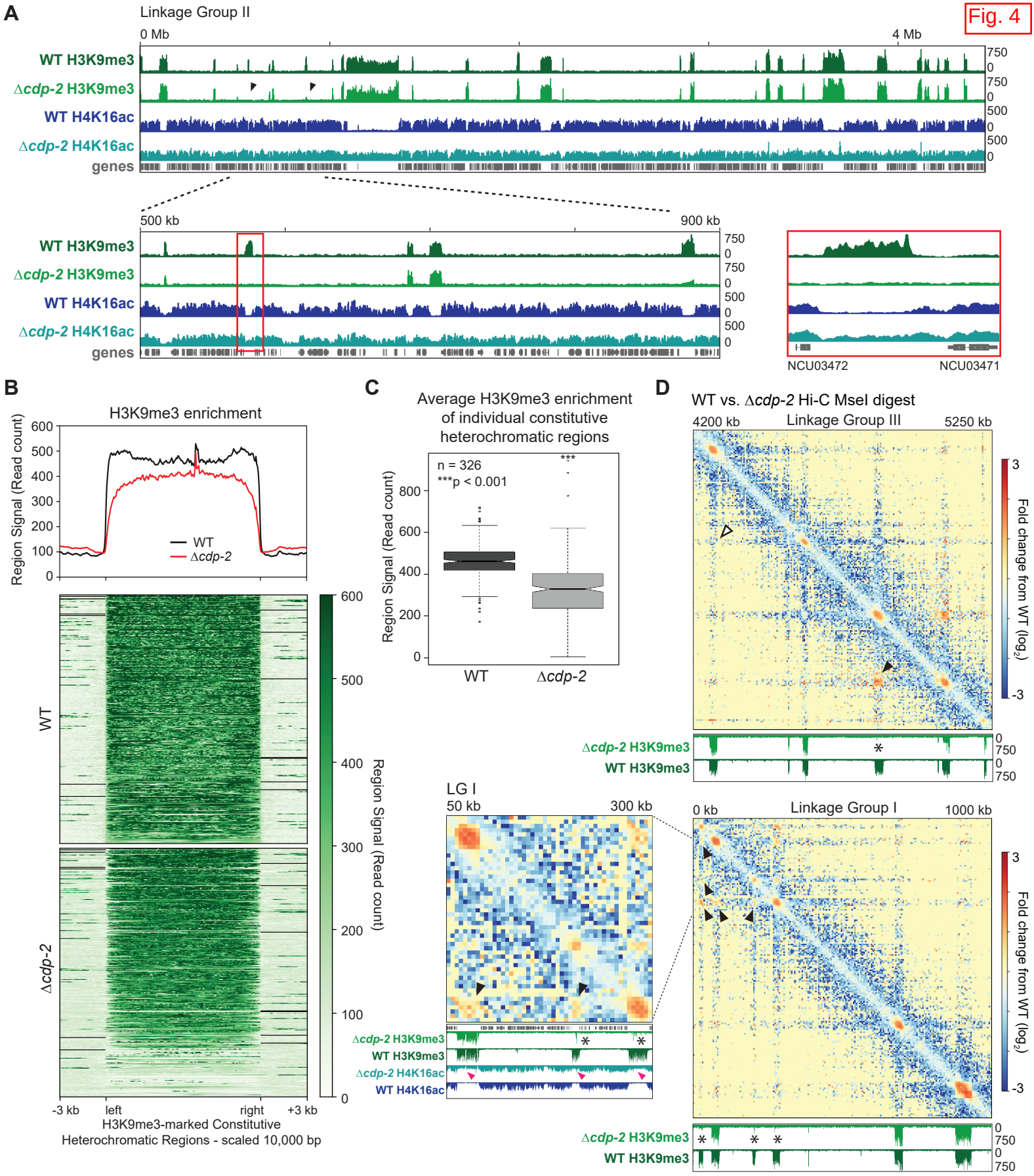
A
Linkage Group II
Fig. 4
0 Mb
4 Mb
WT H3K9me3
Δcdp-2 H3K9me3
WT H4K16ac
Δcdp-2 H4K16ac
genes
750
0
500
0
500 kb
900 kb
NCU03472
NCU03471
B
H3K9me3 enrichment
Region Signal (Read count)
WT
Δcdp-2
H3K9me3-marked Constitutive
Heterochromatic Regions - scaled 10,000 bp
-3 kb
left
right
+3 kb
Region Signal (Read count)
C
Average H3K9me3 enrichment
of individual constitutive
heterochromatic regions
n = 326
***p < 0.001
***
D
WT vs. Δcdp-2 Hi-C MseI digest
4200 kb
Linkage Group III
5250 kb
Fold change from WT (log2)
LG I
50 kb
300 kb
Linkage Group I
0 kb
1000 kb
Δcdp-2 H3K9me3
WT H3K9me3
Δcdp-2 H4K16ac
WT H4K16ac

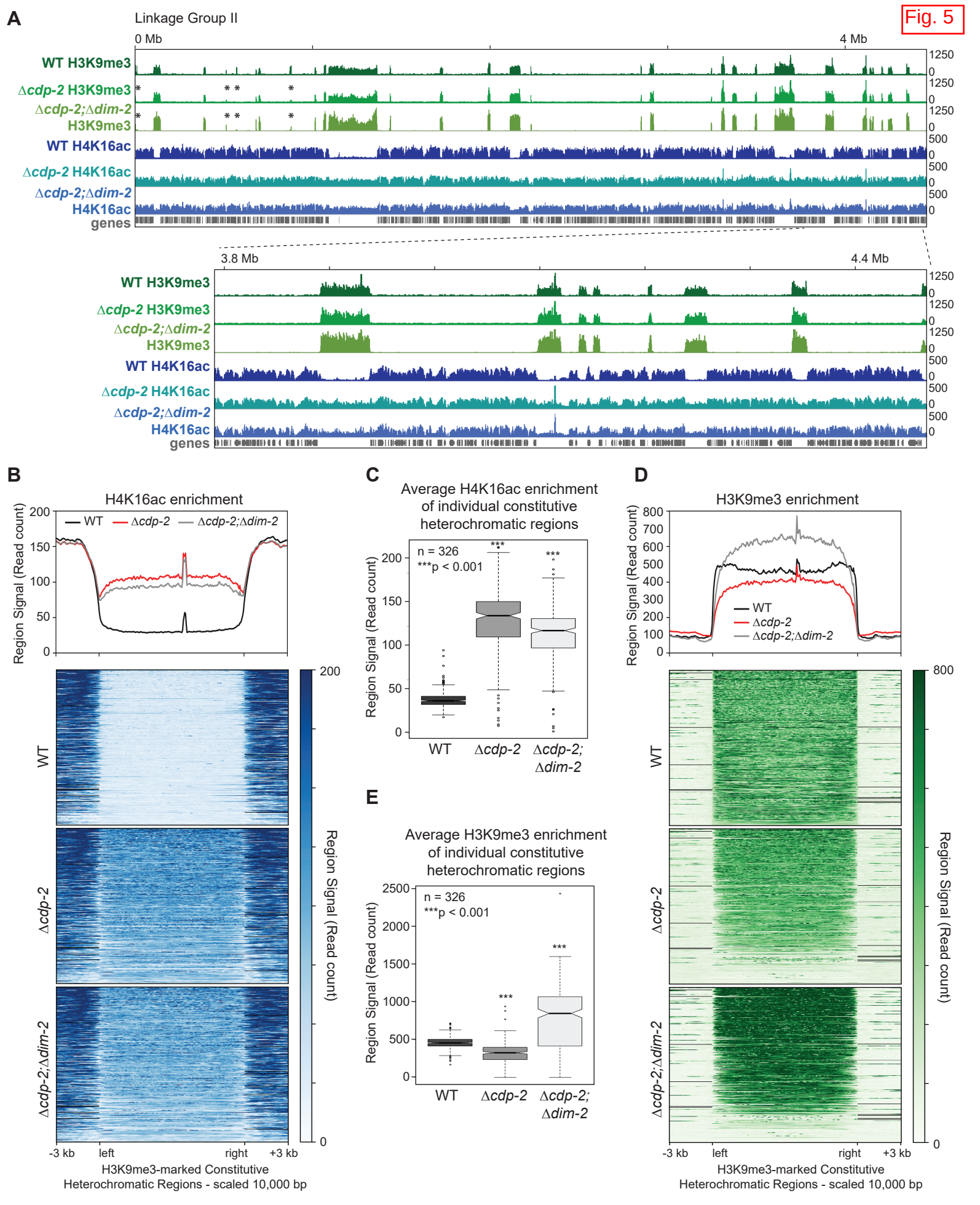
A
Linkage Group II
0 Mb
4 Mb
WT H3K9me3
Δcdp-2 H3K9me3
Δcdp-2;Δdim-2 H3K9me3
WT H4K16ac
Δcdp-2 H4K16ac
Δcdp-2;Δdim-2 H4K16ac
genes
3.8 Mb
4.4 Mb
B
H4K16ac enrichment
WT
Δcdp-2
Δcdp-2;Δdim-2
Region Signal (Read count)
-3 kb
left
right
+3 kb
H3K9me3-marked Constitutive Heterochromatic Regions - scaled 10,000 bp
C
Average H4K16ac enrichment of individual constitutive heterochromatic regions
n = 326
***p < 0.001
E
Average H3K9me3 enrichment of individual constitutive heterochromatic regions
D
H3K9me3 enrichment

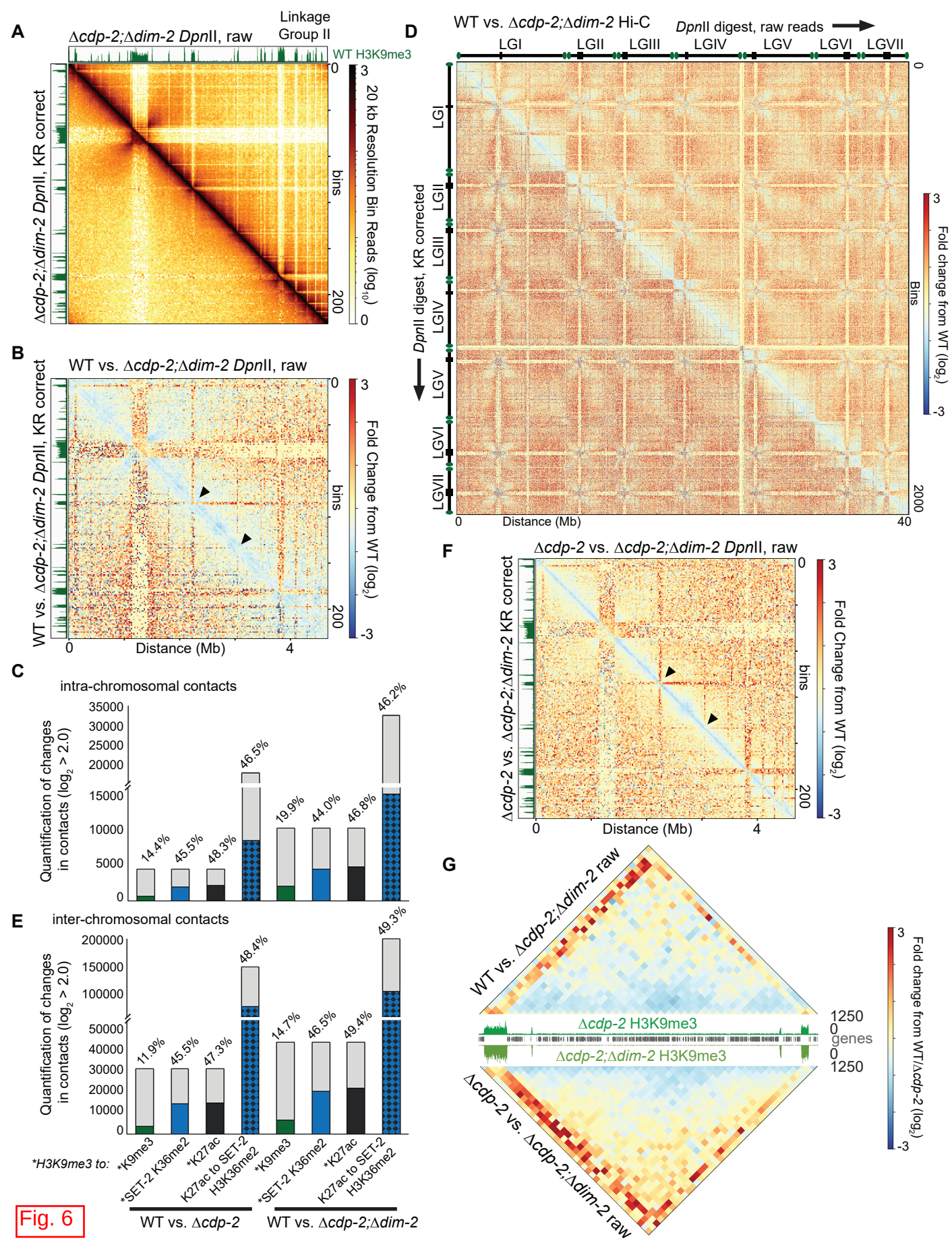
A
Δcdp-2;Δdim-2 DpnII, raw
Linkage Group II
WT H3K9me3
Δcdp-2;Δdim-2 DpnII, KR correct
bins
20 kb Resolution Bin Reads (log10)
B
WT vs. Δcdp-2;Δdim-2 DpnII, raw
WT vs. Δcdp-2;Δdim-2 DpnII, KR correct
Fold Change from WT (log2)
Distance (Mb)
C
intra-chromosomal contacts
Quantification of changes in contacts (log2 > 2.0)
14.4%
45.5%
48.3%
46.5%
19.9%
44.0%
46.8%
46.2%
D
WT vs. Δcdp-2;Δdim-2 Hi-C
DpnII digest, raw reads
LGI
LGII
LGIII
LGIV
LGV
LGVI
LGVII
DpnII digest, KR corrected
Bins
Fold change from WT (log2)
E
inter-chromosomal contacts
Quantification of changes in contacts (log2 > 2.0)
11.9%
45.5%
47.3%
48.4%
14.7%
46.5%
49.4%
49.3%
*H3K9me3 to:
*K9me3
*SET-2 K36me2
*K27ac
K27ac to SET-2 H3K36me2
WT vs. Δcdp-2
WT vs. Δcdp-2;Δdim-2
F
Δcdp-2 vs. Δcdp-2;Δdim-2 DpnII, raw
Δcdp-2 vs. Δcdp-2;Δdim-2 KR correct
G
WT vs. Δcdp-2;Δdim-2 raw
Δcdp-2 H3K9me3
Δcdp-2;Δdim-2 H3K9me3
genes
Δcdp-2 vs. Δcdp-2;Δdim-2 raw
Fold change from WT/Δcdp-2 (log2)
Fig. 6

Fig. 7

A

Wildtype heterochromatin and genome organization

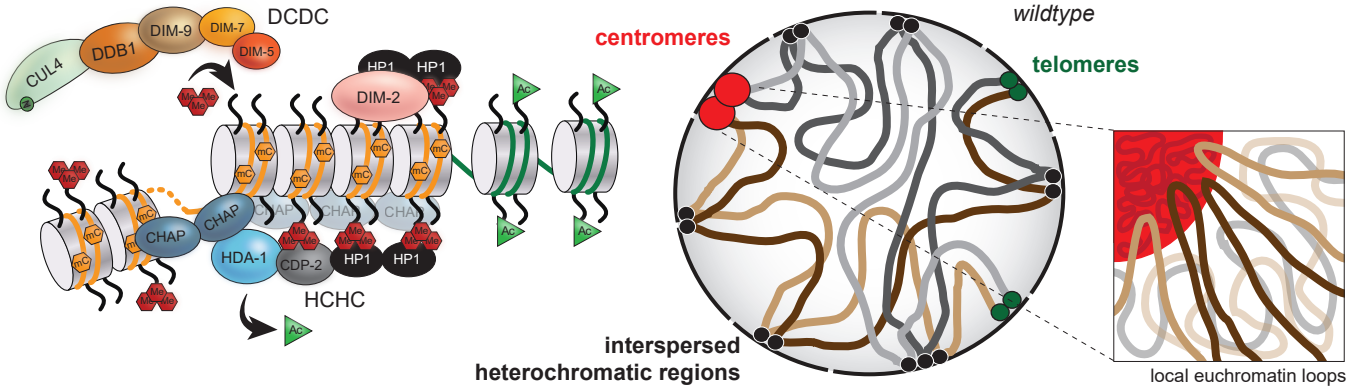

B

HCHC-deficient (Δ*cdp-2*) heterochromatin and genome organization

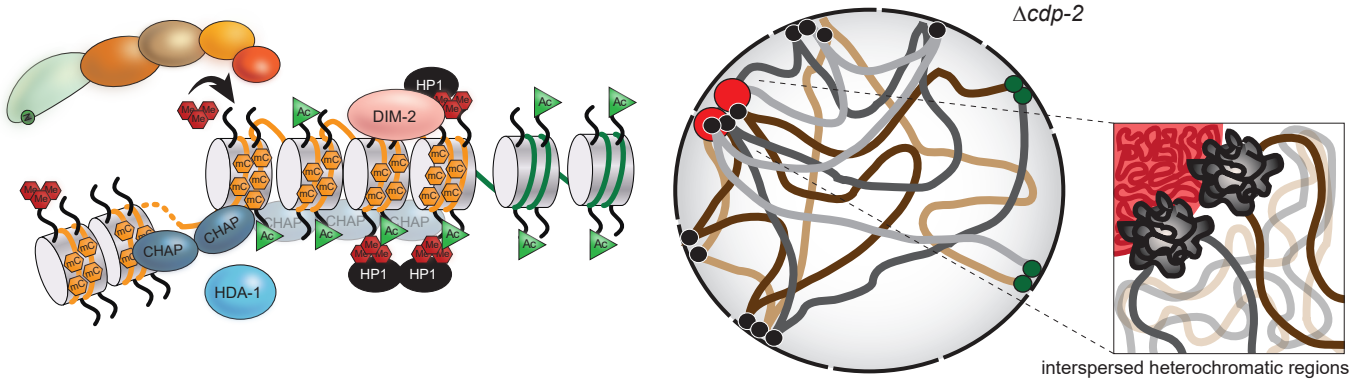

C

HCHC-deficient (Δ*chap*) heterochromatin and genome organization

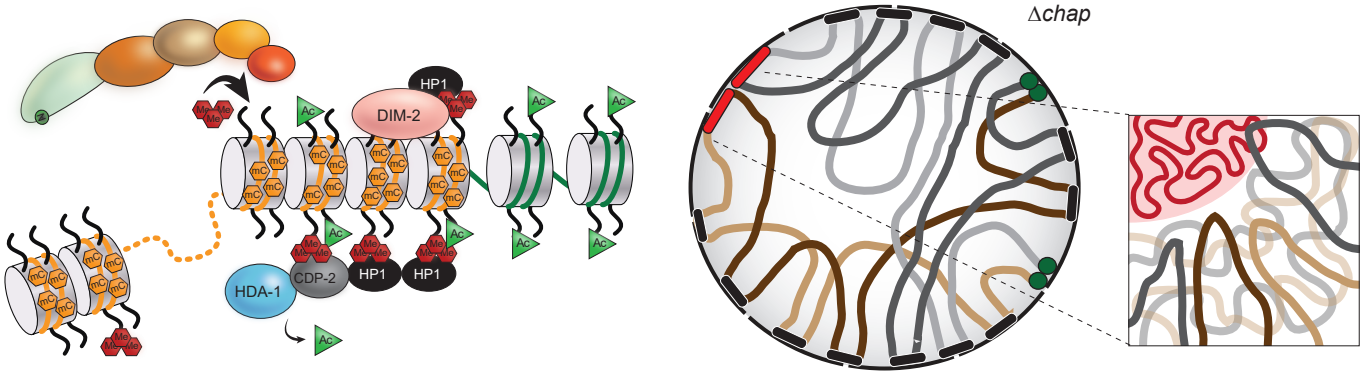

D

HCHC and DNA methylation-deficient heterochromatin and genome organization